University of Crete

Department of Physics

Master Thesis

Characterization and growth of InGaN thin films by the sputtering method

Spyridon Georgakis

Supervisor: *Prof.* Eleftherios ILIOPOULOS

Heraklion Crete

February 2017

MSc THESIS

Submitted in partial fulfilment
of the requirements for the degree of
Master of Science in Micro- / Opto-electronics

Defended by
Spyridon Georgakis

Characterization and growth of InGaN thin films by the sputtering method

COMMITTEE

Prof. Elefterios Iliopoulos

Prof. George Kiriakidis

Prof. Alexandros Georgakilas

Date of the defense: 24/2/2017

Abstract

In recent years, III-nitride semiconductor materials have become promising candidates for use in electronic and photovoltaic devices due to their wide direct bandgap that cover most of the solar spectrum (0.7-3.4 eV) [1]. In particular, solar cells based on group III nitrides have attracted much attention since InGaN has high light absorption coefficients. In this thesis, we study the fundamentals of deposition III-nitride thin films by radiofrequency (rf) reactive sputtering. The aim of this thesis is to investigate the growth of gallium nitride and indium gallium nitride films by RF sputtering that could be used in effective and inexpensive photovoltaic devices. It is imperative to point out that it is the first attempt to deposit III-nitride materials by RF sputtering in the labs of Microelectronics of FORTH/IESL.

It was shown that no probable condensation and pre-cleaning of GaN powder target led to dominated oxynitride and oxide phases in grown thin films. However, we achieved to have a good control on the growth process, as a result, we could initiate growing GaN and InGaN films minimizing the oxygen incorporation in as-deposited samples. Hence, the optical properties of the films were studied by spectroscopic ellipsometry (SE) and the measured data were analyzed by taking into account the effects of surface roughness based on an effective medium approximation model. X-ray diffraction (XRD), Energy-dispersive X-ray (EDX) and Hall measurements were used to characterize the structural and electrical properties of films. The most crystalline GaN films were grown in a pure nitrogen atmosphere, low pressure and high target RF power. The optical bandgap of the optimum GaN films was determined to be approximately 3.4eV. As far as it concerns InGaN films, they were grown having optical bandgaps from 2.91 eV to 2.15 eV. The bandgap was tuning with the RF power and the number of indium pellets onto the target. After alloying with In, the XRD analysis revealed the amorphous phase of InGaN films. A resistivity as low as 0.14 Ω*cm with an electron concentration $3.38*10^{19}$ cm^{-3} and mobility value of 1.55 cm^2/Vs was obtained in $In_{0.3}Ga_{0.7}N$.

Last but not least, it was attempted to deposit p-type GaN and InGaN films with Mg pellets that were placing onto the target. Hall effect measurements showed that when the Mg dopant content in $In_{0.24}Ga_{0.76}N$ increased to 11.5 metallic at. % the as-sputtered film transformed into p-type conduction.

This project was co-funded by the European Union (European Social Fund (ESF)) and the Greek national funds through the Operational Program ‘’Education and Lifelong Learning’’ of the National Strategic Reference Framework (NSRF)-Research Funding Program:THALES.

Acknowledgments

It is a pleasure for me to thank my supervisor, Prof. Eleftherios Iliopoulos, for his support and careful guidance during my studies. His vast knowledge of physics, as well as his ability to simplify the difficult concepts, help me to form deeper insights into physics. Furthermore, it is also important to thank my co-supervisor Dr. Elias Aperathitis for taking the time to guide me all the times I needed his help in sputtering lab and the fruitful discussions we had.
I would also thankful to Kazazis Stelios for helpful remarks during this work, and the implementation of optical measurements. Additionally, I would like to acknowledge Tsagaraki Katerina for EDX measurements. I would like to acknowledge Thanasis Kostopoulos regarding the fabrication of the devices. I particularly would like to thank Mr. Michalis Sfendourakis for technical support at various times during the period of this work.
Last but not least, I would like to express my sincere gratitude to my family and dedicate this thesis to them. It was impossible to achieve this task without the encouragement and the love of my parents.

Contents

1 Introduction 7

2 Theory 8

2.1 Properties of III-Nitrides semiconductors 8

2.1.1 Introduction 8

2.1.2 Crystal structure of Nitrides 9

2.1.3 InGaN alloy 10

2.2 Previous Work 11

3 Experimental Methods 12

3.1 Sputtering method 12

3.1.1 The vacuum system 12

3.1.2 RF-sputtering system 13

3.1.3 Sputtering Yield 17

3.1.4 Sputtering Kinetics and thin film growth 19

3.1.5 Deposition Rate-Target-to-substrate separation 20

3.2 Methods of characterization 21

3.2.1 Spectroscopic Ellipsometry 21

3.2.2 X-ray Diffraction 24

3.2.3 Energy-dispersive X-ray Spectroscopy 25

3.2.4 Electrical measurements 26

4 Experimental Details 28

4.1 Experimental Approach and Preparation of Samples 28

4.1.1 Experimental Approach 28

4.1.2 Optical analysis 29

4.1.3 Preparation for Sputtering 30

4.1.4 Preparation for Hall Measurements 31

4.1.5 Contacts fabrication process 31

4.2 Deposition Conditions and Samples 32

5 Experimental Results 35

5.1 Sputtering GaN **35**

5.1.1 Experimental Approach 35

5.1.2 Sputtering only with Argon 35

5.1.3 Reactive Sputtering 36

5.1.4 Mg-Doping of GaN 47

5.1.5 Alteration of the working distance 50

5.2 Sputtering InGaN **56**

5.2.1 Experimental Approach 56

5.2.2 Bandgap Tuning with RF power and In pellets 57

5.2.3 Mg-Doping of InGaN 59

5.2.4 Electrical Properties of InGaN and Mg-InGaN films 63

6 Conclusions 66

Bibliography 68

CHAPTER 1

Introduction

The III-nitrides have continued to develop as the pre-eminent universal compound semiconductor material which has shown the ability to replace traditional III-V materials in many applications. GaN has many superior material properties compared to other III-V materials; it is mechanically and thermally stable, it can sustain high breakdown voltages (5 x 10^6 V/cm), it exhibits a high saturation velocity (2 x 10^7 cm/s) and when alloyed with indium to form $In_x Ga_{1-x} N$ it has tunable direct bandgap (0.7 eV to 3.4 eV) with a high absorption coefficient of $\approx$1 x 10^5 cm^{-1} [1]. The bandgap of alloy can be tunable by varying the indium at. % and gallium at. % in the InGaN alloy. Additionally, this range of bandgaps makes special InGaN because it can absorb the entire visible spectrum from near infrared to ultraviolet. The ternary InGaN material system offers substantial potential to develop high-performance photovoltaic (PV) devices with reduced cost for terrestrial applications. InGaN solar cells have not yet realized their full transformative potential despite a significant research effort over the last decade. This is due to numerous materials integration challenges that must be solved in order to achieve useful efficiencies and to increase the indium incorporation in InGaN alloys. While high external quantum efficiency has been reported, InGaN solar cells have never exceeded 3% due to many crystal defects and poor device design.

InGaN thin films grown by MOCVD and MBE methods are extensively studied but less is known about deposited films by the RF sputtering method. The purpose of this thesis is to deposit GaN and InGaN thin films by RF reactive sputtering and study their properties. The primary advantages of the deposition method of RF sputtering are a relatively inexpensive and quite effective approach for preparing thin films at low temperatures. Indeed, low growth temperatures must be used to achieve films with high indium content and reduce the desorption of the indium from the surface [2]. At higher deposition rates, incorporation of indium becomes higher [3].

Our task is to deposit InGaN thin films by RF sputtering method and to investigate the electrical, optical and structural effects of deposition parameters. Additionally, the transformation into p-type conduction, as the Mg dopant pellets were added, was a challenge for us.

In chapters 2 and 3 we introduce the reader to the theoretical background. Specifically, we begin with the properties of III-Nitrides and we continue with state of the art in radiofrequency-sputtered GaN and InGaN films. Next, we proceed with the experimental methods introducing the theory of sputtering method, thin film formation and the methods of characterization used to analyze the thin films. Moreover, in chapter 4 we present our series of experiments which are divided per altered growth parameters each time. In chapter 5 we proceed with the presentation of our experimental results and we provide physical explanation for the observed data. In particular, the first half of the chapter 5 is about the preparation of GaN and Mg-doped GaN thin films and the second half of this chapter is about the growth of InGaN and Mg-InGaN films.

Lastly, chapter 6 summarizes experimental results along with citation of our plans for future research.

CHAPTER 2

Theory

2.1 The properties of III-Nitrides Semiconductors

2.1.1 Introduction

Wide bandgap III-nitrides including AlN, GaN, InN, have seen great success in their development especially in the latest century. It is known that many significant problems had to be overcome before these materials could constitute useful devices. The absence of lattice-matched substrates, which lead to high density of dislocations, and low doping efficiency were the most challenging problems. Initially, it was difficult to believe that a material with a dislocation density in the order of 10^8-10^{10} cm^{-2} would become the building material of many viable devices. So, the unique properties of III-nitrides lead to a large area of applications from optoelectronic devices such as high-performance LEDs to high-power electronics. The wide direct bandgap of GaN makes this material useful for both light emitting source and high-temperature applications. GaN and its alloys are promising to form high power electronics such as high-speed field-effect transistors. GaN doesn't possess inversion symmetry since the Ga-N bond has a polar nature. Hence, this property causes the induced polarization to be asymmetric if GaN will subject to an alternating electric field. The intrinsic tendency of III-nitrides is to form a wurtzite structure, which is thermodynamically stable, with a hexagonal symmetry. The strong chemical bonds in III-nitride materials are due to the large difference in electronegativity between the group III elements and nitrogen (Al=1.18, Ga=1.13, In=0.99, N=3.1). This characteristic along with the wide direct energy gap are the origin of impressive properties of III-nitrides. The III-nitrides have energy bandgap energy tunable from 6.2 eV for AlN to 3.4 eV for GaN to 0.69 eV for InN [16].

Additionally, wide bandgap III-nitride semiconductors have much lower leakage and dark currents, which are important for photodetectors and electronic devices. A consequence of the strong chemical bonding is the chemical stability of these materials along with the physical stability such as high melting points, mechanical strength. Furthermore, the III-nitrides have high thermal conductivity and their effective masses are higher than conventional semiconductors, which results in lower carrier mobilities. Finally, their refractive indices are lower compared to narrower bandgap semiconductors, thus leading to lower reflectivity at the interface [16].

2.1.2 Crystal Structure of Nitrides

Group III nitrides can exist in wurtzite , zinc blende and rock salt crystalline structures. The thermodynamically stable phase is that of wurtzite symmetry for bulk AlN, GaN, and InN. Initially, it is widely known that GaN crystallizes in either the cubic structure (zinc blende) or the more stable hexagonal structure (wurtzite). Each of the atoms forms an individual sublattice arranged in a hexagonal close pack system that is shifted along (0001) c-axis by 3/8 of c-lattice parameter. The most common growth direction of hexagonal GaN is normal to the {0001} basal plane, where the atoms are arranged in bilayers consisting of two closely spaced hexagonal layers, one with cations and the other with anions. The anions (N^{3-}) form an hcp structure in which the cations (Ga^{3+}) occupy half of the tetrahedral sites [23]. The wurtzite structure is depicted schematically in Fig. {2.1}. Miller indices (hkil) are used to index atomic planes in the crystal and these indices are based on a coordinate system with 4 axes. There are three basal axes which make 120^0 with each other and the fourth axis (c-axis) is vertical to them [25].

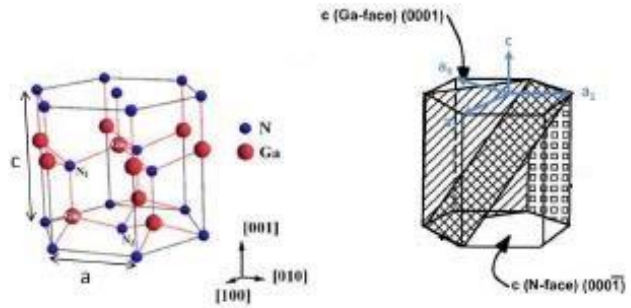

Fig. {2.1}: Wurtzite structure a) atom positions, b) main atomic planes.

Additionally, the wurtzite and zinc blende structures differ only in the bond angle of the second nearest neighbor (Figure {2.2}).

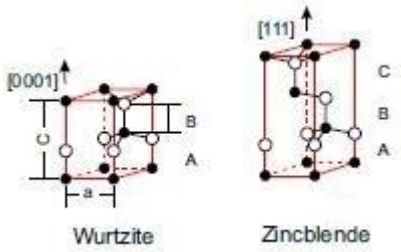

Fig. {2.2}: Stick and ball stacking model of crystal with zincblende structure along [111] direction(left), and with wurtzite structure along the [0001] direction.

Because of the different cations and ionic radii (Al^{3+}: 0.39 $\dot{A}$, Ga^{3+}: 0.47 $\dot{A}$, In^{3+}: 0.79$\dot{A}$), InN, GaN and AlN have different lattice constants as shown in Table {1.1} and bandgaps (Fig.{2.3}).

Wurtzite, 300K	AlN	GaN	InN
a_o ($\dot{A}$)	3.112	3.189	3.537
c_o ($\dot{A}$)	4.982	5.185	5.705
c_o/a_o	1.601	1.626	1.613

Table {2.1}: Lattice parameters of GaN, InN and AlN.

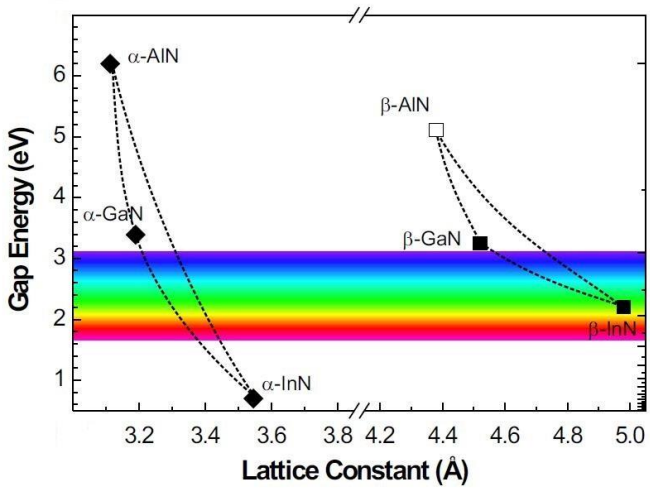

Fig. {2.3} The bandgaps of nitrides versus their lattice constants.

2.1.3 InGaN alloy

InGaN is already an integral part of important device designs. $In_xGa_{1-x}N$ (x is the InN mole fraction) is not any less important than $Al_xGa_{1-x}N$ for the fabrication of electrical and optical devices, such as LEDs and lasers, which can emit in the violet or blue wavelength range. The ability to control the bandgap of InGaN over a range that provides a good spectral match to sunlight, makes InGaN suitable for solar photovoltaic cells [29]. It is possible to grow multiple layers with different bandgaps, as the material is relatively insensitive to defects introduced by a lattice mismatch between the layers [3]. This material, however, is not as easy to grow because of the high vapor pressure of N on In and also mismatch between the large In atom and the small N atom. In order to solve this problem, large V/III ratios, increasing with InN mole fraction, as well as reduced growth temperatures are employed [21].
The compositional dependence of InGaN bandgap is a crucial parameter and the energy bandgap of $In_x Ga_{1-x} N$ can be expressed by the following empirical expression:

$$E^g{}_{In_xGa_{1-x}N} = xE^g{}_{InN} + (1-x)E^g{}_{GaN} - b_{InGaN}(1-x)x = 0.7x + 3.4(1-x) - b_{InGaN}(1-x)x\,.$$

Impurities and dopants

A basic understanding of which elements might act as impurities in group III-nitrides is important for the growth of films and crystals with optimized optoelectronic properties. Atoms with tetrahedral radius close to those of M (M=Ga, Al or In) and N would have a tendency to substitute for these. Hence, if we consider only those impurities which would be isoelectronic or act as single donors or acceptors, we conclude that C, Ti, O and Ge should have a high solubility in the Al and Ga sublattice. On the other hand Si, Zn, In and Mg should have a moderate to low solubility in the Al and Ga sublattice.
Oxygen is a well-known impurity in GaN and its incorporation has a drastic influence on the structural properties of GaN. For oxygen on the Ga site, the atomic geometry is similar to the nitrogen anti-site; oxygen moves towards the inequivalent nitrogen neighbor and forms a strong N-O bond. Within the physically allowed range of chemical potentials and Fermi energies, oxygen on a nitrogen site is the energetically preferred configuration. Substituting nitrogen with

oxygen causes small elastic strain around the defect, because the O-Ga bond length is only 0.5% larger than the bulk Ga-N bond. Oxygen on a N site has one electron level close to the conduction band which is singly occupied in the neutral charge state and therefore acts as a single donor [44].

2.2 Previous Work

This section will focus on particularly relevant work in thin film deposition by the sputtering method. Generally, the reactive sputtering technique has been employed as a plasma-assisted method for the growth of GaN films at low substrate temperatures. The resistivity of GaN films prepared this way is high (10^8-10^{13} Ω*cm), probably because they are strongly compensated by acceptor-like defects. A mixture of molecular nitrogen and argon was used as nitrogen source and sputtering gas. The advantage of plasma-assisted sputtering methods is the low substrate temperature, which enables the deposition of In-containing alloys, the use of substrate materials as Si or GaAs, and the reduction of thermally activated diffusion of dopants and interdiffusion at interfaces of multilayer structures. The disadvantage of sputter processes is that the Ga and In targets are usually easily oxidized [26]. Therefore, these surface oxide layers should be removed by long (several hours) presputtering.

Takayuki et al. investigated GaN films deposited on Si (111) substrates by reactive rf-magnetron sputtering at nitrogen pressures from 0.08 to 2.70 Pa without intentionally heating the substrates [3]. The XRD patterns indicate that the GaN films deposited at pressures lower than 1.1 Pa were polycrystalline highly oriented with the (0001) plane preferred.

E. C. Knox-Davies et al. reported polycrystalline gallium nitride films 100 nm to 1 μm thick, were deposited from 0.15 to 6.0 Pa, at substrate temperatures varied from room temperature to 450 ^{O}C [4]. The most crystalline films were grown at mid-range temperatures and low target biases. Oxygen contamination of 3-30% at. % had a major effect on the optical properties of the films, increasing the bandgap values from 3.02 to >4.0 e V and decreasing the refractive index from 2.46 to 2.03.

Finally, Cheng-Che Li et al. reported $In_xGa_{1-x}N$ films with x=0, 0.25 and 0.5 grown on SiO_2 (50nm)/Si substrates by reactive sputtering at 200 ^{O}C. The RF power was kept at 100 W and the chamber pressure at 9 mTorr. InGaN films showed preferential $(10\bar{1}0)$ diffraction and electron mobility up to 7 $cm^2\ V^{-1}s^{-1}$ [5].

CHAPTER 3

Experimental Methods

3.1 Sputtering Method

3.1.1 The Vacuum System

The vacuum pumping arrangement associated with an r.f. sputtering system has to perform two main functions, to pump the chamber down to a sufficiently low pressure to remove undesirable gases to an acceptable level (typically 10^{-7} torr) and to maintain the vacuum chamber at a pressure of between 10^{-3} and 10^{-2} torr during the sputtering process. During the initial pump down the vacuum pumps have to face the residual gas in the chamber, outgassing from the chamber walls, the targets and the substrates. The ultimate pressure achieved in the vacuum chamber is controlled by the various outgassing rates provided that we don't have leaks. The outgassing rate is measured in units of (torr*l)/sec and is related to the pressure p and the pumping speed S, with constant pressure, by the relation:

$$Q = pS$$

The outgassing rate from the stainless steel cylinder chamber is between 10^{-4} and 10^{-5} (torr*l)/sec. A single 8-inch diameter dielectric target will add a further gas load of up to

$3*10^{-4}$ (torr*l)/sec.

Rotary pump

The size of the rotary pump that backs the diffusion pump usually receives little attention in systems that do not have to operate with a continuous gas bleed. The typical gas load of less than 10^{-4} (torr*l)/sec obtained with a chamber pumped to its ultimate pressure only needs a pumping speed of 10^{-3} l/sec to maintain a pressure of 0.1 torr in backing line.

The function of the rotary pump in its backing role is to maintain the backing pressure, the pressure at the outlet of the diffusion pump, at a level considerably below the critical backing pressure of the diffusion pump. If the critical backing pressure is exceeded the top jet of the diffusion pump will stall and allow large quantities of oil vapor to diffuse up towards the chamber.

Diffusion Pump

The diffusion pump is the most widely used high vacuum pump in sputtering applications because of its proven reliability, simplicity and low cost. Since water vapor is often the major constituent in the gas remaining in the chamber at pressures below 10^{-5} torr, a liquid nitrogen trap should be used in those applications where a low initial partial pressure of water vapor is required. A continuously run liquid nitrogen trap placed directly over the diffusion pump would eventually collect all the diffusion pump oil. Taking the speed of the pumping stack to be 110 l/sec, the ultimate pressure in the chamber will reach 10^{-7} torr. The pumping speed of a 6-inch diffusion pump is about 1300 l/sec at its inlet. Therefore, the maximum gas load that the pump will handle is about 1.3 (torr*l)/sec. All of the gas that enters the diffusion pump will pass into the backing line to be pumped by the rotary pump. The critical backing pressure for a 6-inch diffusion pump is about 0.5 torr. However, the use of a pressure not exceeding 0.2 torr is recommended in order to provide a safety margin. Hence, the pumping speed required at the exit from the diffusion pump is 1.3/0.2= 6.5 l/sec.

Background (base) pressure

The base pressure is the partial pressure of the gases that are not deliberately admitted into the chamber. The main sources of background pressure are outgassing from the chamber, fittings in the chamber, the targets, substrates and impurities in the sputtering gas. Pumping down to a low pressure before admitting the sputtering gas assists in reducing the base pressure. In general, a pressure in the 10^{-6}-10^{-7} range should be reached during pump-down before adding the sputtering gas [28].

3.1.2 RF Sputtering System

Introduction

Sputtering is an atom-by-atom process, the target is bombarded by ions which physically remove atoms off the target causing them to be ejected from the surface and subsequently strike the substrate and adhere. The factors to take into consideration when evaluating sputtering for film deposition are listed below:

- sputtering yields and corresponding deposition rates vary for different metals, alloys and insulators
- films of complex materials can be sputter deposited
- film-thickness control is simple and easily reproduced
- large area targets can be used for sputtering
- the plasma can be manipulated to achieve greater film thickness uniformity. Fast electrons can be kept away from the substrate to prevent substrate heating.

The process

The object of sputtering is to remove material from a target and to deposit the material onto a substrate. The close packed atoms at the surface of the target are subject to bombardment by fast moving atomic sized particles. When the fast-moving atomic particles hit the target surface they cause agitation of the surface atoms to such an extent that some are knocked out of the surface and travel to condense on the substrate. The atoms that leave the target surface can travel to the substrate because both the target and the substrate are contained in a vacuum system where the number of gas molecules is low. If the number of gas molecules is too high, then most of the sputtered atoms will collide with the gas molecules and return to the target. The proper way to obtain a large number of fast atomic sized particles bombarding the target is to immerse the target in a plasma, that contains ions and electrons along with applying a high negative voltage to the target surface. So, the negative voltage attracts the ions from the plasma to the target surface.

Before radio frequency (RF) sputtering was invented, it was considered impossible to sputter insulators because the charge buildup on the insulator target could not dissipated. The RF voltage needs to be capacitively coupled to the target surface. This is implemented by including a capacitor in series with the electrical feed to the target when metal targets are used. The RF diode sputtering system requires an impedance-matcing unit between the RF power supply and discharge chamber. The impedance of the power supply is almost always 50 Ω. The target is normally bonded to a metal backing electrode which can be directly connected to a RF power supply, as shown in figure {3.1}. In this case a RF voltage is induced on the front surface of the target by capacitive coupling through the target [30].

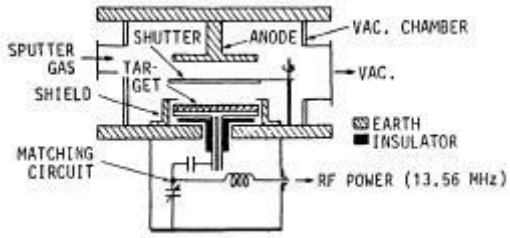

Fig. {3.1}: Radio-frequency diode sputtering system [30].

Generally, with RF potentials it is possible to enhance the negative charge on the target. Electrons are more mobile than positive ions and have a difficulty in following the periodic change in the electric field, therefore more electrons are attracted to the front surface of the target during the positive half of the RF cycle than positive ions in the negative half cycle. The resultant electron current causes the target surface to acquire increasing negative bias voltage during successive cycles. Thus, the potential on the target surface after a few RF cycles can be described as an RF potential with a super-imposed negative d.c. bias. Consequently, the discharge current-voltage characteristics are asymmetric and resemble those of a diode. Finally, the value of the bias potential is close to half of the peak-to-peak RF voltage on the target surface.

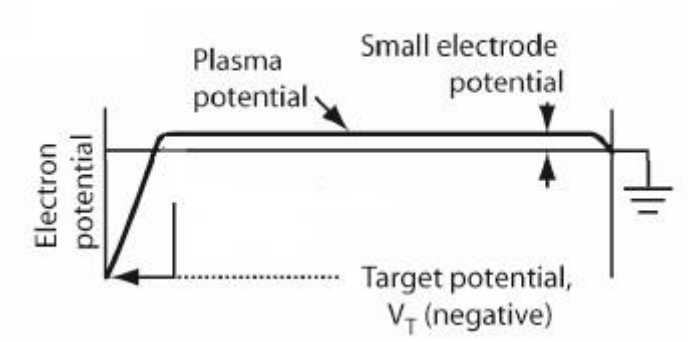

Fig. {3.2}: The potential as a function of distance between the target and the grounded substrate.

The ions from the plasma are accelerated to the target essentially by the bias potential (V_T) and bombard the target with an energy of the order of V_T electron volts. The majority of r.f. sputtering equipment utilizes the r.f. electric field between the target and the substrate to sustain the plasma. Electrons that are released from the target surface by ion bombardment, are accelerated across the sheath in front of the target to energies of up to several keV. These electrons cause some ionization of the low-pressure gas environment as they travel to the work table. At the work table the energetic electrons from the target cause further electrons to be released. These electrons are accelerated into the plasma by the small potential difference always present between any solid surface and a plasma to which it forms a boundary. The energy of these electrons, although generally less than 100 eV, is still sufficient to contribute to the ionization of the gas environment. A small residual RF field present in the plasma also accelerates some of the electrons which are products of ionization to suitable energies for ionization to occur [24].

Finally, all r.f. sputtering electrodes have earthed shielding around their non-active surfaces which carry r.f. voltages and are in the vacuum environment. The purpose of this shielding is threefold. Initially, it's positioned sufficiently close between the shield and electrode and prevents sputtering where it isn't desirable. Secondly, the shielding prevents material from the target being deposited on the insulator which isolates the electrode from ground, the deposition of any metal on the insulator would eventually cause electrical breakdown. Thirdly, the shielding is used to help the fulfillment of an optimum uniformity of deposited film. The substrate surface forms one of the boundaries of the RF discharge and can be considered as an electrode. Ions and electrons flow to this electrode and secondary electrons are emitted. Additionally, the substrate sits at a negative potential relative to the plasma. This potential may be different to that of the substrate table. The potential differences will give rise to electric currents when the substrate is in electrical contact with the table. Films that are deposited on substrates mounted so that they are electrically isolated sometimes exhibit different properties to films deposited on grounded substrates [28].

Plasma formation

When voltage is applied to the target the luminous region of the plasma can be seen to be separated from the target surface to leave a 'dark sheath/space'. Generally, most of the voltage applied to the target is dropped across this sheath as shown in figure {3.3}. Ions in the negative glow of the plasma move around with a random motion. Only those positive ions that enter the sheath region during their random motion are accelerated by the voltage across the sheath and bombard the target.

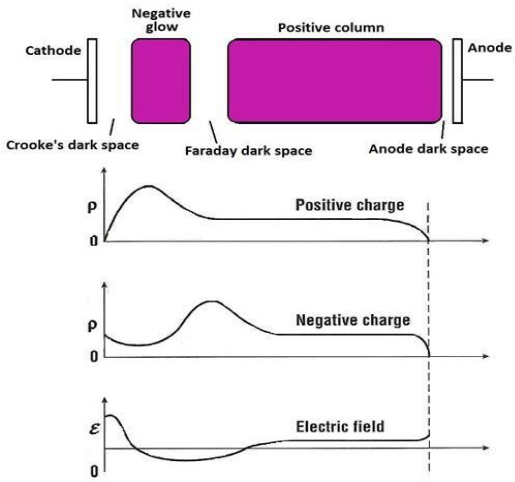

Fig. {3.3}: Positive and negative charge densities, the electric field as a function of distance between the anode and the cathode and the optical emission [Figure taken from [7]].

One of the most outstanding appearances of a glow discharge is the glow itself which is created by relaxation processes of atoms which have been excited by inelastic electronic collisions. The zones which emit light at very different intensities declare that these relaxation processes do not happen with the same intensity across the discharge. Dark areas can be identified adjacent to the electrodes and their extension differs with pressure, power input and type of gas [32].

Figure {3.3} shows the optical properties in the region between the electrodes. The indicated regions of optical emission (glow) are a consequence of high concentration of electrons with moderate energy enough to excite atomic electrons in a neutral atom to higher energy states by inelastic scattering. The excited atoms return to their ground states emitting photons and the electrons are accelerated from the cathode, resulting in a low electron density, compared to ion density, and a net positive charge in the region close to it. In this region, called cathodic (or Crooke's) dark space the electrons don't have the energy to cause optical emission. Faraday's dark space is again relatively dark compared with its adjoining zones, in particular the positive column between this dark space and the anode dark space. The electrons cover the length of cathodic dark space, negative glow and Faraday's dark space gaining enough energy to a least equal the ionization energy or ionization potential. Therefore, this ionization length is proportional to the inverted pressure of the discharge and the potential difference between the electrodes [24].

In the positive column, the gas is in the ideal plasma state which means that the number of carriers equals each other and there is only a very weak longitudinal field. Reducing the distance between the electrodes or decreasing the pressure will affect the nature of the discharge dramatically. Initially, the positive column and Faraday's dark space will vanish. When the

electrodes are so close that the anode dips into the negative glow, the discharge is quenched, if the voltage is not simultaneously increased. Hence, the most important zones of a discharge are Crooke's dark space and the negative glow. The large electric field here causes ions to accelerate rapidly towards the cathode and bombarding the target material [36].

The potential does not vary linearly across the distance between the electrodes. Due to the different mobility of the positively and negatively charged carriers, space charges are built up which change the spatial shape of the voltage in a characteristic way. Specifically, a steep decrease across the cathodic dark space in the cathode fall is followed by a region of constant potential and vanishing field in the negative glow and the electric carriers move randomly. In the positive column, the potential slowly grows [24].

3.1.3 Sputtering Yield

Initially, we can assume that the number of ejected atoms or molecules is proportional to the number of the surface layer atoms which have undergone recoil into the body of the crystal, distinguished into three different zones [Sigmund, 33]. So, in the first regime, the lattice atoms which have just had a collisional impact up to hundreds of eV have got enough energy in order to leave the lattice. On the other hand, this amount is not able to sustain the collision cascade and as a result it is terminated. In the second regime, the collision cascade process occurs at keV range and the lattice atoms in the surface layer of the target are moving chaotically. Moreover, in the third regime of MeV range, almost all atoms are moving simultaneously and therefore it is possible that moving atoms will exchange their momentum. We can say that the collisional cascade is considered as atomic billiards.

In the binary collision approximation, the energy transfer follows the conservation of momentum: $$T = 4\frac{m_i m_t}{m_i + m_t} E_{kin} \cos^2\theta = \gamma E_{kin} \cos^2\theta = T_m \cos^2\theta \qquad (1)$$

with m_i and m_t atomic masses of a projectile ion and a surface atom, E_{kin} the kinetic energy of m_i , and θ the scattering angle.

Energy Spectrum of Sputtered Atoms

It has been established experimentally and theoretically that an energy spectrum of sputtered atoms emerging from a collision cascade, can be fine reproduced by Thompson Formula [8]. This collision cascade it can be generated by high-energy medium-heavy ions and the formula can be expressed in terms of differential sputtering yield Y(E) of atoms sputtered with ejected energy E for incoming ions of normal incidence as $Y(E)\,dE \propto \{\frac{1-\sqrt{\frac{U_S+E}{\gamma E_O}}}{E^2\left(1+\frac{U_S}{E}\right)^3}\}dE$ (2)

where E_o and E are the energies of incident ions and sputtered atoms and U_s is the surface binding energy of a target material, $\gamma = \frac{4M_1M_2}{(M_1+M_2)^2}$ (3)

with M_1 and M_2 are the masses of an incoming ion and target atom [10].

When $\gamma E_o \gg U_s$ and E the equation {2} is approximated by

$$Y(E)\,dE \propto \frac{E}{(E+U_S)^3}\,dE \quad (4)$$

At impact energies significantly below 1 keV deviations from the Thompson formula have been observed in measurements, specifically for light ions through the assumption that sputtered atoms undergo only elastic collisions [10]. It is imperative to point out that the knockout process of a surface target atom executed by an incident light ion becomes dominant at large angles [9]. So, the knockout process at large angles, is divided into direct and indirect ones. The first one means the direct knockoff of a surface atom by an incident ion. As far as the indirect one we mean the knockoff of a surface atom by an incident ion which is scattered just before near the surface by the other target atoms (Fig. {3.4}).

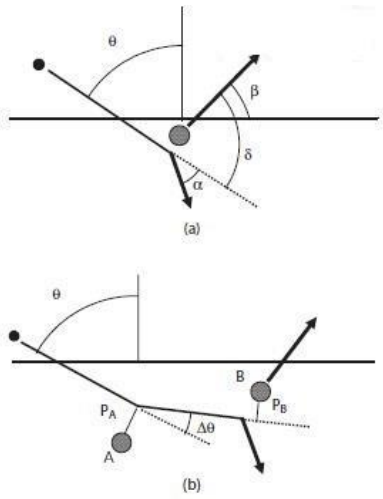

Fig. {3.4}: Schematic diagram of knockout processes by light ions for a) direct knockout process and b) indirect knockout process. [Figure taken from Springer [10]]

3.1.4 Sputtering Kinetics and thin film formation

Here we will describe the processes and the individual mechanisms that occur during the formation of a film by condensation from the gaseous phase. During the surface diffusion, the deposited atoms move to the surface with an average diffusion length depending on their kinetic energy at the time of growth. Moreover, nuclei can be formed by different crystalline phases of the deposited material depending on local pressure and temperature conditions of the substrate surface, a process called nucleation. The growth of the crystallites after the phase of nucleation requires the formation of nuclei in a critical dimension. In the process of sputtering, energetic atoms from the gas phase are incident on the film and may detach surface atoms. Hence, the increased temperature results in higher mobility of atoms at the interface of film with substrate which creates the smoothing interfaces. Finally, the growth process of the film is to adsorb the deposited atoms to the nuclei and the islands of the grown material. Condensation of the grown material from the gas phase is determined by the incident rate of atoms on the surface of substrate and this rate equals to

$$R = \frac{p}{\sqrt{2\pi MkT}} \tag{5}$$

where p is the partial vapor pressure of the grown material, the molecular weight M, k the Boltzmann constant and T the temperature. When an atom is adsorbed could be evaporated directly or be subjected to surface diffusion. This surface diffusion can be restricted from the kinetic energy of the deposited atoms, or from the rest of the mechanisms mentioned above in this chapter. Ultimately, we can conclude that the growth of thin films is a process far from thermodynamic equilibrium.

.

3.1.5 Deposition Rate-Target-to-substrate separation

The rate with witch material is deposited in a RF sputtering system is often considered to be important. Although high deposition rates appear to be desirable in order to reduce the total time for the growth of the film, the use of high rates should be viewed with caution since unsatisfactory film properties may result.

Generally, the rate of erosion of a particular material on the target electrode will increase as the amount of RF power applied to the target electrode is increased. If we make the approximation that the rate of erosion of material from the target is uniform across it, then

$$E = \gamma P \tag{6}$$

where E is the erosion rate, γ is a constant and P is the power density at the target surface.

The material that is emitted from the surface of the target is emitted in all directions. The amount of material that is emitted in any direction is described by the known cosine law, the amount of material emitted in any direction at an angle Θ to the normal surface is proportional to $\cos(\Theta)$. Because of this erosion characteristic some of the material from the target will not arrive on the area of the substrate. The rate of arrival of material at the center of the substrate is GE, where G is a dimensionless geometrical factor which can be calculated from the equation:

$$G = \left(\left(\frac{h}{R}\right)^2 + 1\right)^{-1} \tag{7}$$

where h is the target to substrate separation, R is the radius of the target and G is the ratio of the rate of deposition at the substrate to the rate of erosion at the target [28].

In most vacuum deposition process not all of the material that reaches to the substrate remains, but is re-emitted from the substrate surface. The re-emission coefficient ρ is the ratio of the amount of material leaving the substrate to the amount arriving. Additionally, the amount of material re-emitted from the center of the substrate is ρGE and the net deposition rate D. Assuming a uniform rate of re-emission across the substrate, the rate can be multiplied by the geometrical factor G to ρEG^2, as the rate of arrival of the re-emitted material at the center of the target. The net sputtering rate S is related to the erosion rate by:

$$S = E(1 - G^2\rho) \tag{8}$$

The deposition rate D is equal to:

$$D = GE(1 - \rho) \tag{9}$$

3.2 Methods of characterization

3.2.1 Spectroscopic Ellipsometry

Ellipsometry is a thin film measurement technique that uses polarized light. It is a very sensitive surface technique, greater than a simple reflection measurement that derives from the determination of the relative phase change in a beam of reflected polarized light. Generally, the spectroscopic ellipsometry is carried out in order to determine thin film thicknesses and thin film optical constants.

The use of spectroscopic measurements provides much more information about the sample, and provides the acquire data in spectral regions where the measured data are most sensitive to the model parameters which are to be determined. In many cases the dispersion of the optical constants of a given material is known, or the optical constants may be parameterized in such a way as to enforce some type of dispersion on the optical constants (Cauchy, Lorentz and parametric semiconductor models). Ellipsometry measures the change in polarized light upon light reflection on a sample. Fundamentally, ellipsometry uses the fact that linearly polarized light at an oblique incidence to a surface changes polarization state when it is reflected, as shown in Fig. {3.5} [22].

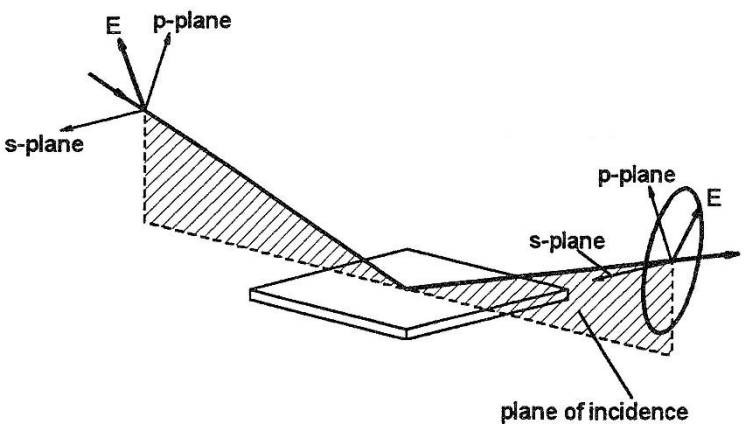

Fig. {3.5}: The general principle in ellipsometry [22].

More specifically, when a monochromatic plane light wave is directed at a surface at oblique incidence, the plane of incidence is defined as a plane perpendicular to the surface and containing the vector which points in the direction of propagation of the light wave. This vector is called the wavevector k_{in}. Furthermore, perpendicular to k_{in} are the two perpendicular vectors, the one for the electric field E and the other one for the magnetic field B of the light wave. The vector of electric field is decomposed into two components, which are mutually perpendicular and perpendicular to k_{in}. Additionally, the two components of E are respectively parallel and

perpendicular to the plane of incidence. So, the vectors are named, ‘’Parallel’’ (π) and ‘’Senkrecht ‘’ (σ).

The incident light wave is linearly polarized. When the light wave reflects off the surface, the polarization changes to elliptical polarization. This means that the amplitude and mutual phase of the π- and σ-component of E are changed making the endpoint of E to move in an ellipse [22]. The ellipsometric parameters can be related to the reflection coefficients of the light polarized parallel and perpendicular to the plane of incidence R_p and R_s , respectively. The relation is the basic equation in ellipsometry and is given by the complex ratio ρ of the two Fresnel reflection coefficients

$$\rho = \frac{R_p}{R_s} = \tan(\Psi)e^{i\Delta} \tag{10}$$

The ellipsometric parameters ψ and Δ, which are the measured values, are given by a measurement with an ellipsometer and the two reflection coefficients are functions of the complex refractive index of the material. Additionally, the ellipsometric angles Ψ and Δ are defined as $\Psi = \tan^{-1}|\rho|$ and $\Delta = \Delta_p - \Delta_s$ the differential phase change. So, the Ψ and Δ can be used to determine the sample’s optical parameters. Lastly, the angles Ψ and Δ determine the differential changes in amplitude and phase, respectively, experienced upon reflection by the vibrations of the parallel and perpendicular electric field vector components.

General procedure for optical experiments

A general procedure is followed in order to extract the desired sample parameters such as thickness, optical constants etc. Thus, we have to solve the inverse problem of modeling the measured data to estimate the values of the sample parameters which best match the measured data. This procedure may be divided into the following four steps, as illustrated in Figure {3.6} below.

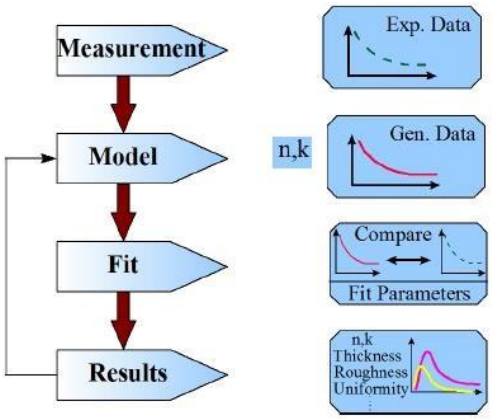

Fig. {3.6}: The procedure for optical experiments [figure from J. A. Woollam Co[22]].

The sample is measured and we have data for polarization states and by measuring the optical quantities Ψ and Δ we can derive the values of the physical parameters. Hence, we build an optical experiment and measure polarization states (ellipsometric Ψ and Δ), as functions of the light beam wavelength, angle of incidence and polarization state. Furthermore, a model should

be established from which we can accurately predict what we should measure from a sample of known properties. This model should contain some known parameters, such as the wavelength of the incident light, the incident beam polarization state and the angle of incidence. However, the model also contains some unknown physical parameters, such as layer thicknesses and some optical constants. So now we can generate data until we find a set of optimized parameters that yield calculated data that subsequently match our measured optical data. Therefore, the abovementioned parameters can represent the true physical structure of the sample under study. Finally, we conclude that many statistical quantities can be calculated in order to evaluate the accuracy and precision of the fit results [22].

Optical absorption

The main optical properties of a semiconductor are typically its refractive index n and its extinction coefficient k or absorption coefficient a . Equivalently, we mean the real and imaginary parts of the relative permittivity. It is widely known that refractive index decreases as energy bandgaps of semiconductors increases. The refractive index and the extinction coefficient are related by the Kramers-Kronig relations. Hence, large rise in the absorption coefficient for hv near and above the bandgap E_g results in augmentation of refractive index versus hv in this region [11].

The excitation of an electron from the valence band to the conduction band by an absorption of photon is called band-to-band absorption. So, the band-to-band absorption are always one of two types, direct and indirect transitions. In direct transition the photoexcitation process no phonons are involved. Hence, when the photon is absorbed, the electron's wavevector does not change during the excitation of an electron from the valence band to the conduction band.

The absorption coefficient (a) is related to the quantum-mechanical probability of transition from an initial energy (E) to the final energy, the occupied density of states at (E) in the valence band from which electrons are excited, and the unoccupied density of states in the conduction band at E+hv. Near the band edges, the density of states can be approximated by a parabolic band and the absorption coefficient have a following relation with photon energy

$$ahv = A^{*}\left(hv - E_g\right)^{1/2} \tag{11}$$

where the constant $A^{*} \approx \frac{e^2(2\mu^{*})^{3/2}}{ncm_e^{*}h^2}$ (12)

where μ^{*} is a reduced electron and hole effective mass, n the refractive index and E_g the direct bandgap. Ultimately, in indirect bandgap semiconductors, the photon absorption for photon energies near the bandgap require the absorption and emission of phonons during the absorption process.

3.2.2 X-Ray Diffraction

X-Ray diffraction (XRD) is a useful, non-destructive technique that can reveal several important properties of thin films [12]. Diffraction is due essentially to the existence of certain phase relations. It is widely known that two rays are completely in phase whenever their path lengths differ by an integral multiple of the wavelength of the beams. Differences in the path length of various rays arise when we consider how a crystal diffract X-rays. Figure {3.7} illustrates the diffraction of a beam of parallel and monochromatic X-rays of wavelength λ which incident on a crystal at an angle θ (Bragg angle), which is measured between the direction of the incident beam and the crystal plane under consideration. Consequently, all reflected components can interfere constructively in phase if this distance is a multiple of the wavelength. This condition for efficient reflection is called Bragg's law:

$$2d sin\theta_B = n\lambda \tag{13}$$

Where n is an integer and d is the lattice spacing. As a result of the periodicity of the lattice, for a monochromatic x-ray beam, a detector finds peaks in reflected x-ray intensity for Bragg angles of incidence that depend on the lattice spacing which is characteristic for a particular plane direction in a crystal phase of a particular material. These peaks carry very useful information about the structure of the measured sample. Since sinθ cannot exceed unity, the basic condition nλ<2d must be satisfied to obtain any diffraction. If λ is much smaller than d, the diffraction angles are too small to be conveniently measured.

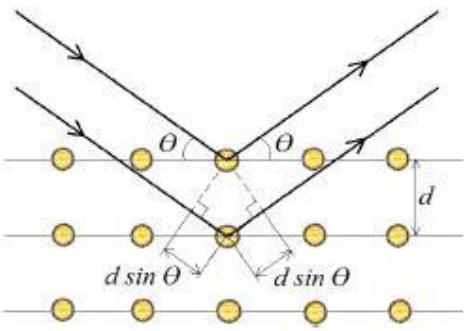

Fig {3.7}: Diffraction of X-rays by a crystal.

Experimentally by using X-rays of known wavelength λ and measuring θ one can determine through Bragg's law the spacing d of the set of planes in a crystal.

So, θ is the angle between the incident beam and the sample, while 2θ is the angle between the incident and diffracted beams, as shown in Fig. {3.8}. In a so called 2θ/θ scan, the sample moves by angle θ and the detector simultaneously moves by angle 2θ.

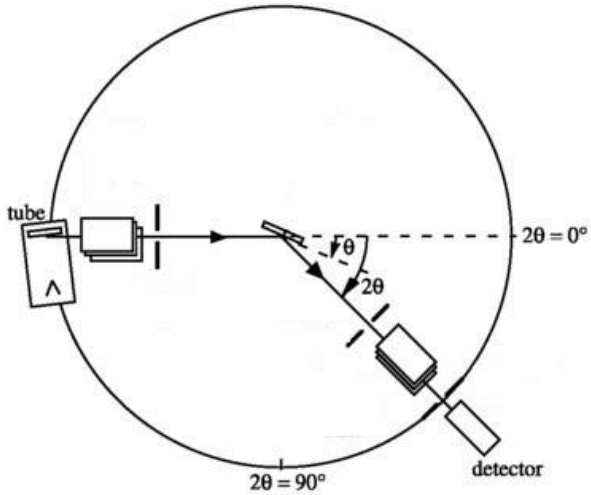

Fig. {3.8}: Schematic setup of a XRD measurement system.

The full width of the Bragg reflection at half-maximum intensity (FWHM) can be used to estimate the size of the crystallites contributing to the reflection. The Scherrer equation relates the peak FWHM to the crystallite size:

$$D = \frac{K\lambda}{\beta cos\theta} \tag{14}$$

(λ) represents the x-ray wavelength, K is the shape factor, (β) is the line width (FWHM) in radians, (θ) is the Bragg angle and (D) is the crystallite size.

3.2.3 Energy-dispersive X-ray spectroscopy

Energy-dispersive X-ray spectroscopy (EDX) is an analytical technique which is used for the elemental analysis or chemical characterization of a sample, and it is used in conjunction with scanning electron microscopy. The EDX technique detects x-rays emitted from the sample during bombardment by an electron beam to characterize the elemental composition of the analyzed volume. Its working mechanism is based on the fundamental principle that each element has a unique atomic structure allowing unique set of peaks on its X-ray spectrum. When the sample is bombarded by the SEM's electron beam, this high-energy electron beam may eject electrons from the atoms consisting the sample's surface. Furthermore, the resulting electron vacancies are filled by electrons from a higher state, and X-ray photons are emitted. This energy is equal to the energy difference between the two electrons' states. This energy of the emitted X-rays is characteristic of the atomic structure of the emitting element. The EDX detector measures the relative abundance of emitted x-rays versus their energy. Finally, the spectrum of x-ray energy versus counts is evaluated to determine the elemental composition of the sample [27].

3.2.4 Electrical measurements

Hall effect measurement

The Hall effect measurement technique has found wide application in the characterization of semiconductor materials since it gives the resistivity, the carrier density and the mobility of carriers. Hall found that a magnetic field applied to a conductor perpendicular to the current flow direction produces an electric field perpendicular to the magnetic field and the current [34].

We can consider a rectangular shaped sample of single carrier type conduction with four contacts in the edges. An electric field $\mathbf{E_z}$ is applied resulting to a current flow $\mathbf{J}_z$ through the sample from the side A to B. According to the figure {3.9} the electrons are going from right to left and the holes in the opposite direction. Uniform magnetic induction $\mathbf{B_x}$ perpendicular to the current flow is also applied. Electrons and holes flowing in the semiconductor will experience a Lorentz-force bending their orbits and they will build up on one side of the sample. An electric field starts to form which counteract the Lorentz-force. After short time equilibrium is reached and no current is flowing in the x-direction I_x=0. The counteract voltage is so called Hall voltage V_H=V_C-V_D . Here, we assume that all the conduction carriers have the same drift velocity v_d and the same relaxation time τ_c according to Drude relaxation approximation. If a hole or an electron is moving in magnetic field a Lorentz force is influenced on them:

$$\vec{F} = q(\vec{v_d} x \vec{B}) \tag{16}$$

Where (q) is the elementary charge. The vector of the Lorentz force has the same direction and amplitude for both carrier types, $|\vec{F_B}| = ev_z B_x$.

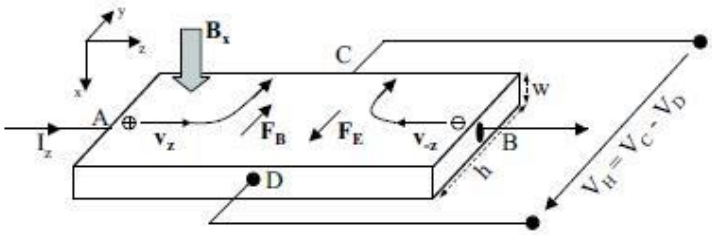

Fig. {3.9}: Schematic illustrating the Hall effect.

The carriers are attracted to the side C, where they cause an electric field, which opposes the force of magnetic field. $|\vec{F_E}| = eE_y$

In steady state the whole force is equal zero, $F_B + F_E = 0 \Rightarrow ev_z B_x = -eE_y$ (17)

Expressing the drift velocity using the current density equation $|\vec{J_z}| = ev_z p$ for holes and $J_z = qnv_{-z} = -env_{-z} = env_z$, $|\vec{J_z}| = J_z = env_z$ (18)

for electrons, where p and n is the bulk hole and bulk electron concentration respectively. From (17) and (18) we get $R_H = \frac{1}{en_H} = \frac{-E_y}{J_z B_x} = \frac{V_C - V_D}{hJ_z B_x} = \frac{V_H}{hJ_z B_x} = \frac{hwV_H}{hI_z B_x} = \frac{wV_H}{I_z B_x}$ (19)

where n_H could be either n or p , R_H is the Hall factor, V_H the Hall voltage, h the layer width and w the conductive layer thickness. If the Hall voltage is negative, then the conduction is caused by electrons and if V_H>0 by holes.

According to the contact's numeration shown in Fig. {3.10} the Van der Pauw resistivity can be defined as: $R_{ij,kl} = \frac{V_k - V_l}{I_{ij}}$ (18)

where (I) current enters the sample through contact (i) and leaves through (j) and $V_{kl}=V_k-V_l$ is the voltage between contacts (k) and (l). If we implement all the possible permutations, the resistivity can be defined as:

$$\rho = \frac{\pi w}{8ln2}[(R_{21,34} - R_{12,34} + R_{32,41} - R_{23,41})f_A + (R_{43,12} - R_{34,12} + R_{14,23} - R_{41,23})f_B]$$

where f_a and f_B the correction factors.

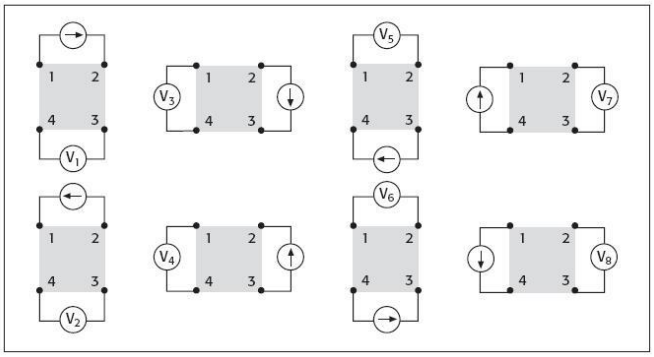

Fig. {3.10}: Van der Pauw arrangement.

For the Hall effect measurement, the current flows through the sample and on the remaining two contacts the Hall voltage is measured, applying a magnetic field. Thus, for different current and magnetic field polarity we get the Hall factor

$$R_H = \frac{w}{8}\left(R_{31,42}^{+B} + R_{13,42}^{+B} + R_{42,13}^{+B} + R_{24,13}^{+B} + R_{13,42}^{-B} + R_{31,42}^{-B} + R_{24,13}^{-B} + R_{42,13}^{-B}\right)$$

Therefore, the carrier concentration can be calculated by $n = \frac{1}{eR_H}$, if R_H>0 we have p-type conductive semiconductor and for R_H<0 n-type.

Finally, the mobility of the sample can be calculated by $\mu = \frac{1}{en\rho}$.

CHAPTER 4

Experimental Details

4.1 Experimental Approach and Preparation of Samples

4.1.1 Experimental Approach

In this thesis, thin films were deposited by an RF reactive sputtering technique under sputtering gas mixtures ($Ar+N_2$). In preparing the films RF (13.56 MHz) sputtering equipment (Nordiko Ltd) was used with a water-cooled 99.98% pure gallium nitride target, produced by American Elements, 10.16 cm in diameter and 6.3 mm thick. The sputtering target was bonded to 20.32 x 1.14 cm copper (Cu) backing plate with plug. The system was evacuated by a 110 l/sec diffusion pump achieving a base pressure $<6.5*10^{-7}$ Torr prior to each run to avoid oxygen contamination. The substrate was kept at room temperature without external heating. Finally, the target-to-substrate distance was fixed at 9.9 cm except the last two series of experiments which was fixed at 5.5cm.

The crystal structure of the films was analyzed by the x-ray diffraction (XRD) method using a *Rigaku D/MAX-2000*H diffractometer with Cu Ka radiation (λ=1.54 A) from a source operated at 40 kV and 82 mA.

Optical properties of the thin films, in this thesis, were studied in detail employing variable angle spectroscopic ellipsometry(VASE). Optical dielectric functions of polycrystalline GaN thin films were obtained from the analysis of the spectroscopic ellipsometry data acquired using a rotating analyzer VASE J.A. Woolam Co. Measurements were performed at room temperature in the photon energy range of 1.22- 5.98 eV with 250 meV step. The angles of incidence of the light beam on the sample surfaces were chosen to be 65^0, 70^0 and 75^0. A sophisticated parametric semiconductor model was used to simulate the measured SE spectra below and above the fundamental bandgap of GaN. In addition, Cauchy model was also used to analyze the SE spectra below the fundamental bandgap of GaN.

Scanning electron microscope (SEM) scans the as-sputtered sample surface with a high-energy electron beam which in turn interacts with the atoms of the sample. Thus, signals produce including secondary electrons, characteristic X-rays and backscattered electrons that contain information about the sample's topography, composition etc. Additionally, SEM set-up have also an additional unit, the Energy-dispersive x-ray spectroscopy (EDS) which is used for elemental analysis of thin films. During EDS analysis, to avoid charging effects that can arise from glass substrates, films grown on silicon substrate are used.

Electrical properties of the samples deposited on glass substrates were investigated by resistivity and Hall effect measurements in Van der Pauw configuration at room temperature

and a magnetic field of 0.32 T. A Hall system based on Keithley K7065 Hall card was employed. In most cases the measurements were performed in high resistivity mode (with input impedance >100 TΩ). Due to the current source (Keithley K224) employed lower current supply limit of 10 n A and the required upper limit (2 V) of applied voltage, when using the high resistivity mode, only samples with sheet resistance below 200 MΩ/□ could be measured.

4.1.2 Optical analysis

In order to derive the optical constants of nitride films, a physically analytical expression for their description has to be employed in the process of fitting the ellipsometric data. The VASE experimental data were analyzed using a four-layer model consisting of: a) Si (100) substrate, b) SiO_2 layer of 2-3 nm thickness above the substrate, c) the polycrystalline GaN or amorphous InGaN thin film, and d) the surface roughness layer. This model structure used to fit the SE data taken on all films and hence obtained the index of refraction (n) and the extinction coefficient (k). The surface roughness layer was chosen as an over layer to obtain accurate optical constants and a good fit to the experimental data. The surface roughness was modeled using a Bruggeman effective medium approximation (EMA) consisting of 50 % of the film and 50% voids. In the case of amorphous InGaN compound semiconductors the Cody-Lorentz model was selected since it provides an accurate description for the below-band gap region (Urbach-tail) which is pronounced in these polycrystalline films [13].

In the Cody-Lorentz model, the imaginary part $\varepsilon_{2CL}(E)$, of the complex dielectric function

$\varepsilon_{CL}^{*} = \varepsilon_{1CL}(E) + i\varepsilon_{2CL}(E)$, is parameterized by seven parameters {E_0, E_p, E_t, E_u, E_g, A, Γ}. The parameters A and Γ are the Lorentzian peak amplitude and width respectively. The parameter E_t separates the point, below which the absorption coefficient is described by an exponential decay strength, with width E_u namely the Urbach tail. Above E_t, the absorption coefficient is described by a Lorentzian absorption peak, centered at E_o, suitably modified at the lower energy region to represent a parabolic absorption regime with optical band gap E_g. Lastly, E_p corresponds to the transition energy point between the parabolic and the purely Lorentzian absorption regimes. As far as the real part $\varepsilon_{1CL}(E)$ of the dielectric function is deduced from Kramers-Kronig transformation of the imaginary part. On the other hand, in the case of oxides and GaN films the Herzinger-Johs Psemi model was used to derive the optical constants. The refractive indices {n} below the bandgap can be represented by a slowly varying function of wavelength such the Cauchy model. The Cauchy model is defined as

$$n(\lambda) = A + \frac{B}{\lambda^2} + \frac{C}{\lambda^4}$$

where A, B and C are fitting parameters and λ is the optical wavelength.

EMA model

There are lot of models in the literature for the calculation of the effective optical constants of a mixture of two or three materials, known as effective medium approximations (EMA). The simplest EMA is to simply linearly interpolate between the constituent optical constants, as shown in the following equation

$$\tilde{\varepsilon} = f_A\tilde{\varepsilon}_A + f_B\tilde{\varepsilon}_B + f_C\tilde{\varepsilon}_C$$

Where $\tilde{\varepsilon}$ is the effective complex dielectric function of the mixture f_A, f_B, f_C are the volume functions of each constituent material ranging from zero to one, and $\tilde{\varepsilon}_A, \tilde{\varepsilon}_B, \tilde{\varepsilon}_C$ are the complex dielectric functions of the constituent materials. The volume fractions must total unity and the above equation is valid for three constituent EMA models. In this thesis, Bruggeman EMA model was used to model a wide range of mixing effects. Specifically, this model makes the choice of the host material complex dielectric function equaling the final effective complex dielectric function of the multi-constituent material. The Bruggeman EMA analysis can be expressed as the following two equations:

$$f_v\frac{\varepsilon_v-\varepsilon}{\varepsilon_v+2\varepsilon} + f_N\frac{\varepsilon_N-\varepsilon}{\varepsilon_N+2\varepsilon} + f_o\frac{\varepsilon_o-\varepsilon}{\varepsilon_o+2\varepsilon} = 0 \ ,$$

$$f_v + f_N + f_o = 1,$$

where f_v, f_o, f_N are the functions of voids, oxide and nitride respectively.

In the case of Ga(O)N thin films, when oxygen concentration was high, we applied EMA model in order to identify how dense or porous was each film. Moreover, the quantification of proportion of GaN phase, in the films, is possible through EMA model. It is crucial to point out that the abovementioned used model consists of GaN, Ga_2O_3 and voids.

4.1.3 Preparation for Sputtering

The thin films were deposited on Corning glass and silicon (100) p-doped substrates. Before the deposition, the substrates were cleaned after cutting to remove dust and grease particles. This was done by wiping with acetone followed by 15 minutes submerged in acetone with ultrasonic agitation and afterwards in isopropanol sequentially. Then all the substrates were rinsed in flowing deionized water in order to remove traces of the organic solution and dried using compressed nitrogen gas spray before being placed in the sputtering chamber.

4.1.4 Preparation for Hall Measurements

Samples for Hall measurements were deposited on square glass slides cut to dimensions of 0.5 cm by 0.5 cm. The 4 probes of the Hall setup were placed around the perimeter of the sample, after the four edges of the sample were soldered with indium dots forming Ohmic contacts. The upper method could give us a first order approximation for the magnitude of the resistivity of the samples. Furthermore, in the last series of experiments the bulk of the glass substrates was patterned with Hall patterns by optical lithography in order to perform accurate electrical measurements. This high precision procedure offers symmetric Greek crosses mounted periodically along the sample. The geometry of the Hall patterns is shown in Figure {4.1}.

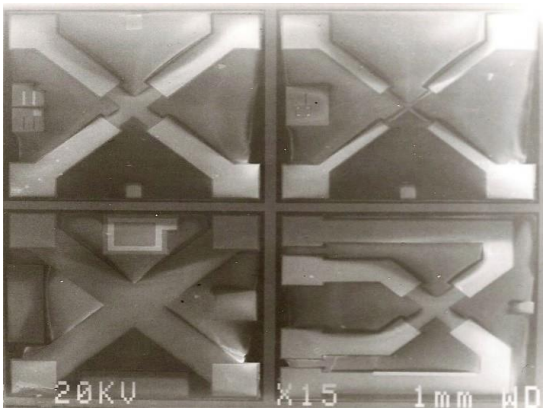

Figure {4.1}: *The geometry of Hall patterns.*

4.1.5 Contacts fabrication process

A standard semiconductor processing technique was used for the fabrication of ohmic contacts. Briefly, the samples were first etched by reactive ion plasma etching (RIE). N-type ohmic contacts of Ti (50 nm)/Au (150 nm) were deposited by electron-beam evaporation on the etched surface. Cr (30 nm)/Au (120 nm) were electron-beam deposited as the p-type ohmic contacts.

4.2 Deposition Conditions and Samples

The 43 samples deposited in the course of this work, could be divided into six different series of performed experiments depending on the process parameters varied; as shown in Tables {4.1-4.5}, which are the following:

- **1st series: Sputtering of GaN on Ar plasma**
  In this series of experiments, three samples were deposited as trial runs and the two process parameters varied was the rf power, which was varied from 100 up to 200 W, and the total sputtering pressure.

Sample	Pre-cleaning (min)	Power (Watt)	Pressure (mTorr)	Gas
S1644	5 [Ar]	100	5	100 % Ar
S1645	5 [Ar]	100	3	100 % Ar
S1646	5 [Ar]	200	5	100 % Ar

Table {4.1}

- **2st series: Reactive Sputtering**
  In the second series of experiments, the nitrogen flow ratio [$N_2/(N_2+Ar)$] was controlled as a growth parameter from 50% to 100%.
  The process pressure was varied from 1.7 to 10 mTorr and the target was conditioned for different duration and gases prior to each deposition.

Sample	Pre-cleaning (min)	Power (Watt)	Pressure (mTorr)	Gas
S1647	5 [Ar]	200	5	50 % Ar 50% N_2
S1648	5 [Ar]	300	5	50 % Ar 50% N_2
S1653	5 [Ar]	300	5	10 % Ar 90% N_2
S1654	30 [N_2]	300	5	10 % Ar 90% N_2
S1655	5 [Ar]	300	5	100% N_2

S1656	5 [Ar]	300	10	10 % Ar 90% N_2
S1661	30 [N_2]	300	10	40 % Ar 60% N_2
S1662	30 [N_2]	200	10	40 % Ar 60% N_2
S1663	30 [N_2]	200	10	10 % Ar 90% N_2
S1664	30 [N_2]	300	10	100% N_2
S1665	30 [N_2]	300	10	10 % Ar 90% N_2
S1666	30 [N_2]	300	2	100% N_2
S1678	30 [N_2]	300	1.7	100% N_2
S1679	30 [N_2]	300	2	100% N_2
S1680	30 [N_2]	300	2	20 % Ar 80% N_2
S1681	30 [N_2]	300	2	100% N_2
S1682	30 [N_2]	300	2.5	100% N_2
S1683	30 [N_2]	400	2	100% N_2
S1685	30 [N_2]	400	2	100% N_2
S1687	30 [N_2]	500	2	100% N_2
S1689	30 [N_2]	500	2	100% N_2

Table {4.2}

- **3rd series: Mg-Doping of GaN**

  In order to deposit Mg-GaN films, pellets of Mg were added. The process was carried out in pure nitrogen atmosphere and the total sputtering pressure was fixed at 2 mTorr. Standard presputtering conditions were set as follows: pre-cleaning at 9.5 mTorr for 1 hr in pure nitrogen atmosphere, pre-sputtering pressure was reduced to 5 mTorr for 3 hrs and the last one hour prior the growth, the nitrogen pre-sputtering pressure was fixed at the working pressure of each growth.

Sample	Number of Mg pellets	Power (Watt)
S1696	2	400
S1697	2	500
S1698	2	550
S1699	4	550

Table {4.3}

- **4th series: Alteration of the working distance**

  In the fourth series, the separation distance between the substrate and the target was changed from 9.9 cm to 5.5 cm. The RF power and the working nitrogen pressure are summarized in the table {4.4}.

Sample	Power (Watt)	Pressure (mTorr)
S1700	400	2
S1701	400	9
S1702	400	4
S1703	550	3.5
S1704	550	4
S1705	600	4.25
S1706	600	5
S1707	600	2.25

Table {4.4}

- **5th series: InGaN thin film deposition**

  In the last series of experiments, In pellets were added in order to deposit InGaN films. Furthermore, InGaN films were doped with Mg to achieve p-type Mg-InGaN film since Mg pellets were placed on the target, and the nitrogen sputtering pressure was fixed at 2.25 mTorr.

Sample	Number of In pellets	Number of Mg pellets	Power (Watt)
S1711	6	-	550
S1712	6	-	600
S1713	6	-	650
S1714	6	3	650
S1715	10	-	650
S1716	7	6	650
S1717	7	10	650

Table {4.5}

CHAPTER 5

5.1 Sputtering GaN

5.1.1 Experimental Approach

Initially, the existence of powder target requires the examination of target. This is crucial in order to have a clean target without porous structure. The condition of target depends on various factors such as the duration of pre-cleaning, addition of reactive gas and the partial pressure (or the flow rate) of gas. Therefore, the chosen approach was to initially determine the pre-sputtering conditions for having non-oxidized and dense compounds on the first layers of the target. At the same time, it was needed to specify the sputtering conditions for depositing high quality films of GaN. The quality of thin films was to be judged via the key factors of the refractive index of films and the quality of crystallinity. The important sputtering parameters were the RF power delivered to the target, the plasma gas flow rate and the addition of nitrogen gas in the plasma. Once the optimum deposition parameters had been found, doping with Mg was performed, varying the number of Mg pellets, in order to attempt to grow samples with p-type doping.

5.1.2 Sputtering only with Argon

In the first series of experiments, three samples were deposited as trial runs. Firstly, the effects of the power supplied to the GaN target were investigated. Increasing the target power should also add to the surface mobility since the sputtered atoms arrive at the surface with more kinetic energy. If the RF power is increased, it will have as a consequence the increasing of the deposition rate.

So, the first two samples were too thin, near to 10-15 nm thickness of films, shown that the deposition rate in 100 W RF power was too low. The third deposited thin film in 200 W was 55 nm thick and the deposition time was endured 1 hr. The deposited films in pure Ar are rich in oxygen at 76% in atomic percentage from EDX results, porous and amorphous. The oxygen was considered to be incorporated into the thin films during sputter deposition process, and the most likely source of oxygen contamination was either from residual oxygen in the deposition chamber or from the GaN sputter target. Lastly, this will be investigated in the next series of experiments.

5.1.3 Reactive Sputtering

In the second series of experiments, it was discovered that the target might have a porous structure consisting of tapered crystallites separated by voids. It is hoped that the introduction of N_2 might reduce the concentrations of the gallium oxide phase, perhaps improving the crystallinity. The chamber was initially vacuum pumped to a pressure below 7 x 10^{-7} Torr. The target-to-substrate distance was 9.9 cm. In this series of experiments, the three process parameters varied were the sputtering pressure, the nitrogen flow ratio [$N_2/(N_2+Ar)$] and the RF power. The sputtering pressure was varied from 2 to 10 mTorr.

The effects of adjusting N_2 gas flow rate along with the presence only nitrogen gas in the process of pre-cleaning were investigated next. This directly affects the surface of the powder target decreasing its porosity. It is well known that plasma treatment is beneficial for activation and cleaning the surface of a porous material. It allows to change not just the surface of the material but also the surface inside the pores. Due to high energetic ions, molecules of plasma can penetrate deep into the voids. After a gradual addition of N_2 gas, GaN target was nitrided. This effect corresponds to increase of the nitrided area on the target surface and as a result higher sputtering rate of GaN species. Nitridation of the target was witnessed by increase of DC bias voltage. The highest deposition rate was reached at the partial pressure of N_2 within 9.5 – 10.5 mTorr. The equilibrium between high-nitridation and cleaning processes was reached at 5 mTorr, since with further increasing of N_2 flow rate the DC bias was decreased.

Gases that are inert in ambient conditions (molecular N_2) become reactive, which undergoes chemical reactions with materials in contact, when present in a plasma discharge due to collisions with energetic particles and subsequent dissociation into atomic neutral (N) and charged (N^+, N^-, N_2^+) components. Once reactive gas is introduced into a process chamber it reacts with the unpassivated, such as sputtering target and chamber walls. The production of atomic nitrogen in N_2 discharges has been shown to result primarily from the following reaction $N_2^+ + N_2 \rightarrow N_2 + N + N^+$ [14]. Electrons in the plasma at 13.56 MHz are extremely ''hot'' having an energy of 2-8 e V at the range of 300-650 W [15]. So, N_2 dissociates/ionize in RF plasma and is reactive under these conditions. Furthermore, molecular nitrogen does not chemisorb on GaN due to the strong N-N bond in the N_2 molecule. Thus, atomic N has to be provided. Nitridation proceeds through different target states as a function of partial pressure of reactive gas and time as is shown schematically in figure {5.1}.

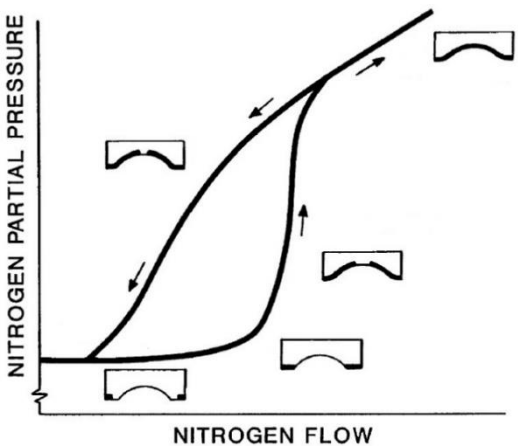

Figure {5.1}: *Target nitridation during pre-cleaning in pure nitrogen atmosphere [20].*

The comparison of two samples would drive us extracting a safe conclusion. We kept the same deposition conditions, the RF power was fixed at 300 W, total pressure at 5 mTorr and the nitrogen flow rate at 90%, the only difference was the pre-cleaning process. The pre-cleaning in pure nitrogen atmosphere led to a drop of 20% the percentage of oxygen in the thin film (from EDS results) in comparison with the deposited film S1653 in which the target was cleaned in Ar plasma prior the deposition. S1654 was less porous but still amorphous, however the amelioration in deposited material was proved by the increase of the refractive index 'n' (figure {5.2}) along with the decrease of optical bandgap. After this run, visual observations showed that the surface of the target was colored grey; thus, a strong indication of nitridation on the target.

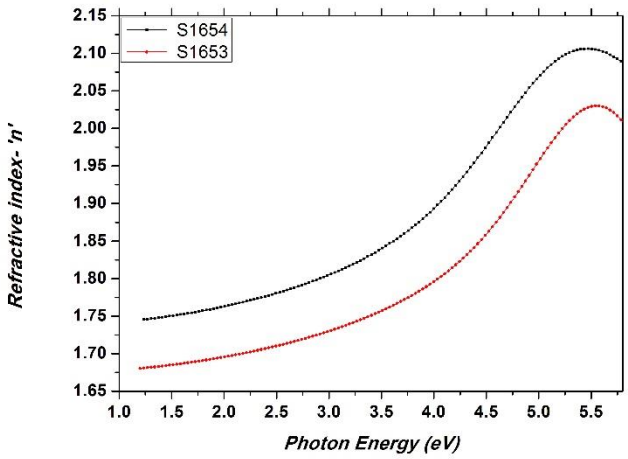

Figure {5.2}: *Typical refractive index curves for the GaON films denoted S1653 and S1654.*

The refractive index and the extinction coefficient of the films were measured with an ellipsometer. Refractive index of the as-sputtered films was lower than that of polycrystalline gallium nitride, based on which one may predict that the films are indeed mixed phases of GaN, Ga_2O_3, and/or gallium oxynitride phases, as shown in Fig. {5.2}.

Figure {5.3} shows a plot of the square of the absorption coefficient times the photon energy times the refractive index $(aE_{ph}\,n)^2$ versus the photon energy (E_{ph}).

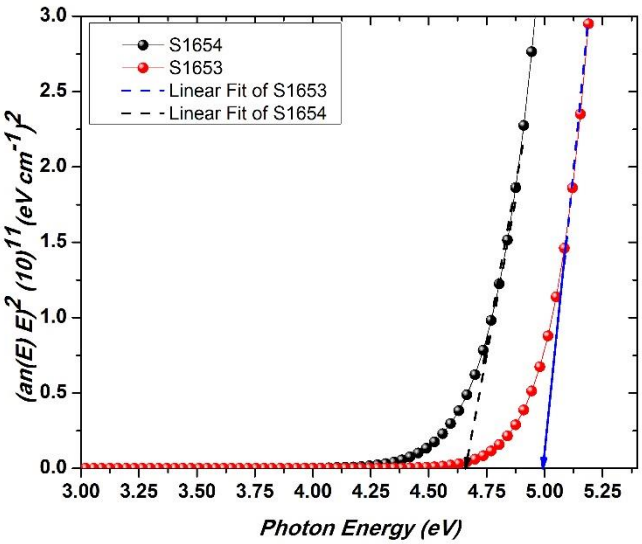

Figure {5.3}: *Plot of (a*n*E)^2 versus photon energy for the optical bandgap determination.*

As can be seen, the plot yields a straight line in the high-energy region, which is indicative of a direct bandgap transition. The *a* absorption coefficient can be calculated from the below equation:

$$a = \frac{4\pi\kappa}{\lambda}$$

where λ is the wavelength of light and k the extinction coefficient.

The optical bandgap {E_g} of the films can be obtained by extrapolating the linear portion of the graph to $(aE_{ph}\,n)^2=0$. The optical bandgap of S1654 sample reveals the high composition in oxygen and the domination of gallium oxide phases in the film.

Furthermore, the increase of deposition rate indicates the nitridation of the target before the deposition, along with the enhanced nitrogen incorporation (see Table {5.1}).

Sample	Pre-cleaning (min)	[N_2/(N_2+Ar)] (%)	Dep. Rate (nm/min)	O (at.%)	E_g (eV)
S1653	5 [Ar]	90	0.84	67.3	5.00±0.12
S1654	30 [N_2]	90	1.05	54.0	4.65±0.11

Table {5.1}: Growth data for GaON films grown at different pre-sputtering conditions, oxygen concentration in the as-sputtered films and their optical bandgaps.

The next step was to determine the optimum N_2 flow rate and working pressure, keeping the parameters of pre-cleaning and RF power constant. The deposited thin film (S1666) was dense without voids. This could be a result of improved nitridation of target along with the formation of dense compound layers on the target. The deposition was carried out at low pressure, 2

mTorr, reducing the deposition rate to 0.65 nm/min. It's imperative to say that the oxygen concentration was found at 29% from EDX results and the refractive index was close to 2.04 at 3.4 eV (see Fig. {5.4}) increased but still far from the reported values 2.35-2.60 for polycrystalline gallium nitride.

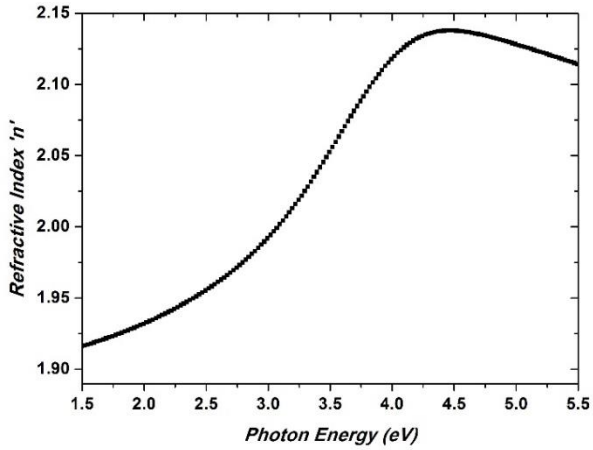

Figure {5.4}: *Refractive index curve for the GaON film denoted S1666.*

Figure {5.5} shows the determination of the optical bandgap energy of sputtered S1666 sample and the value of it was found 3.96±0.11 eV. This improvement was attributed to the growth of gallium nitride phases along with the inexistence of voids.

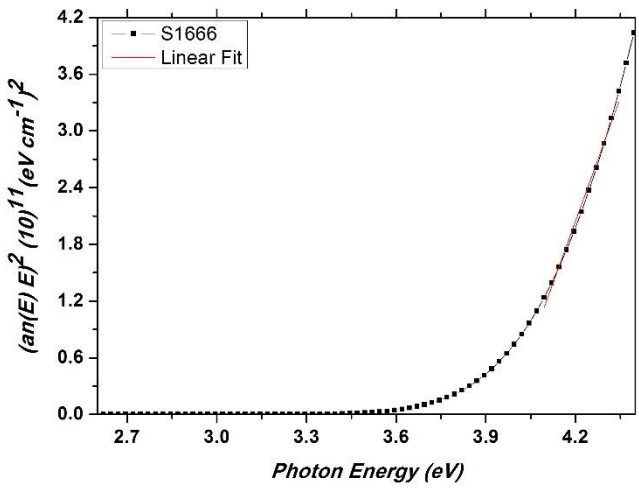

Figure {5.5}: *Plot of $(a*n*E)^2$ versus photon energy for the GaON film denoted S1666.*

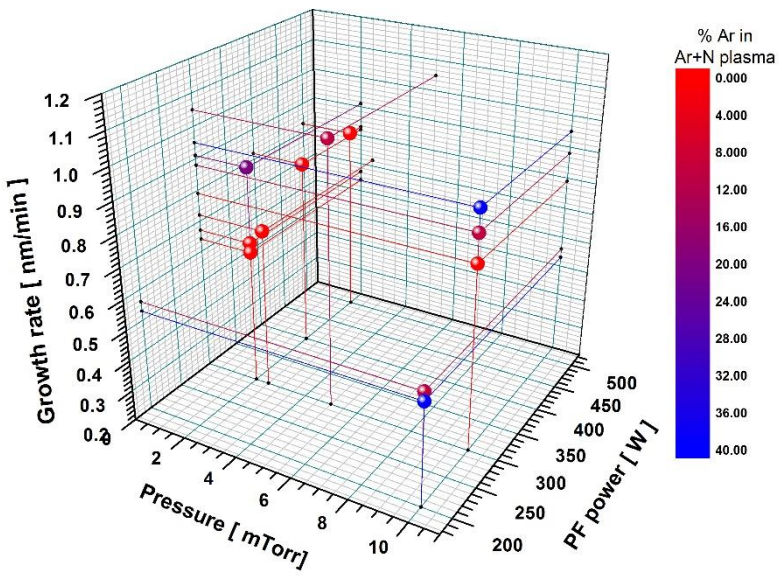

Figure {5.6}: *Plot of relative growth rate as a function of gas pressure and RF power, with different relative oxygen concentration in films.*

In Figures {5.6} and {5.7} the growth rate and the ex-situ oxygen content (data of [O]/([O]+[N]) concentration taken from EDS results) are shown for a number of films deposited at different conditions (gas pressure, RF power and % Ar in plasma phase).

We can clearly observe that there is no obvious correlation of relative oxygen concentration with growth rate (see Fig. {5.6}). The increased growth rate in the same RF power doesn't mean that at the same time oxygen content in as-sputtered films drops. Thus, the existence of more reactive species in plasma is necessary, results in dense films with lower oxygen concentration.

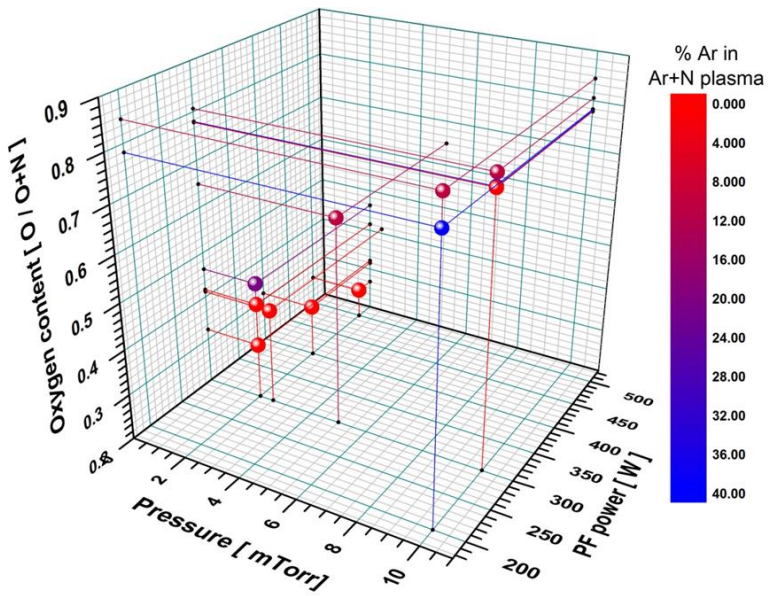

Figure {5.7}: *Plot of relative oxygen content O/[O+N] as a function of gas pressure and RF power, in different gas composition.*

From Figure {5.7}, we can conclude that atomic concentration of oxygen and O/[O+N] ratio can be controlled by mainly varying the sputtering pressure and to a lower degree by varying RF power and gas composition. Keeping only N_2 reactive/sputtering gas, decrease in N_2 partial pressure and subsequently sputtering pressure decreases the oxygen content in thin film. Taking into account the abovementioned, it is accepted that the low sputtering pressure, 2 mTorr, is the most important process parameter which leads to the deposition of dense thin films of gallium nitride with mixed phases of gallium oxide or/and oxynitride, in the specific sputtering system. We have to turn our attention to the energy of the sputtered species from the target. Thus, this energy is low enough not to cause damage or resputtering, but at the same time high enough energy to promote crystal growth. Hence, the atoms/molecules diffuse and find their correct positions in the lattice and if the sputtered species are allowed to reach the growing film with a substantial fraction of their energy, this would create favorable conditions for good crystalline growth. Additionally, the atoms themselves would deliver energy at the surface and help other atoms to surface diffuse, as a result improving the adatom mobility [33]. From basic kinetic gas theory, it can be shown that the mean free path of the atoms in the gas phase can be given by

$$\lambda_{mf} \approx \frac{5\ mTorr * cm}{P\ [mTorr]}$$

Hence, when sputtering at low pressures the atoms don't lose much of their original energy through collisions and they remain energetic in the growth process.

Until now, the EDS spectra have shown that the films are mainly composed of oxygen except S1666 sample. Thus, we suggested the addition of a shield determining the level of oxidation which came from the chamber walls. The aluminum anti-contamination shield was placed surrounding the target and the substrate in order to reduce contamination from the chamber walls on which were oxidized layers. However, the amount of oxygen in next samples found to drop slightly. Hence, it was obvious that the highest percentage of oxygen contamination originated from both gallium nitride target and vacuum environment. Ultimately, all the above results denote the existence of strong correlation with growth conditions of low sputtering pressure since the more energetic plasma leads to dense and lower oxygen content in samples.

The optimum sputtering pressure and the gas flow of pure nitrogen were determined in the previous experiments. The next step was to determine the optimum pre-cleaning conditions and the optimum rf target power, keeping all other parameters constant. The RF target powers used and the pre-deposition conditions are summarized in table {5.2} along with the oxygen contents in as-sputtered thin films. Lastly, the thickness of samples was ranged from 100 up to 120 nm.

Sample	**Pre-Sput. P (mTorr)**	**P_{RF} (W)**	**Dep. Rate (nm/min)**	**O (at.%)**
S1683	2	400	0.82	27.33
S1685	2	400	0.77	27.01
S1687	2	500	0.90	23.78
S1689	9.5	500	0.82	23.29

Table {5.2}: Pre-growth, growth data for GaN films grown at different RF power and oxygen concentration in the as-sputtered films.

As the RF power was increased to 500 W the amorphous peak split into a broad peak, an indication of formation of gallium nitride. As indicated in Figure {5.8} a XRD peak is seen at $2\theta=33.82^0$. This diffraction angle lies between the values expected for (111) planes of zinc-blende GaN and (0002) planes of hexagonal wurtzite GaN.

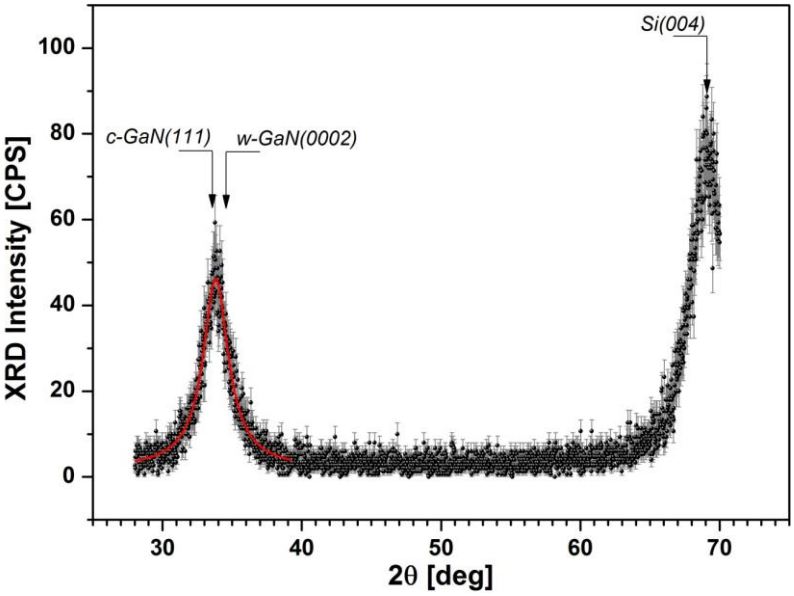

Figure {5.8}: *XRD diffraction pattern of GaN film denoted S1687.*

The structural properties of the samples are summarized in table {5.3}. The grain size {D} was calculated from the FWHM using equation {13}.

Sample	P_{RF} (W)	D(±0.1) (nm)	FWHM (deg.)
S1687	500	3.9	2.17

Table {5.3}: *Summarized XRD results for GaN sample denoted S1687.*

Furthermore, the XRD data reveal that from the Ga(O)N films we didn't take XRD peaks. The amorphous structure of these as-sputtered films remained as the relative oxygen concentration was higher than 0.30. The abovementioned results indicate that GaN films with improved crystalline quality were obtained for rf power beyond 500 W. Ngyen H. Tran et al. [35] suggested a structural model in which the coordination of Ga atoms is dependent on the atomic concentration of oxygen, illustrated in Figure {5.9}. The model consists of a growing Ga-tetrahedral unit with three in-plane Ga-N bonds and an out-of-plane dangling bond parallel to the (002) axis (Fig.{5.9a}). For the films with an oxygen content lower than 25 at. %, an oxygen atom will form an out-of-plane Ga-O bond, leading to formation of the GaN_3O tetrahedral structure (Fig.{5.9b}). This formation is expected not greatly influence the bulk structure and result in formation of well-defined hexagonal structure. However, the GaN_3O structures would lead to the distortion of the bulk, resulting in residual stress. The increase of oxygen concentration to 40% lead to an octahedral structure and the films (Fig.{5.9c}) are looking amorphous in XRD terms. It's evident that this model agrees with our as-sputtered GaN thin films.

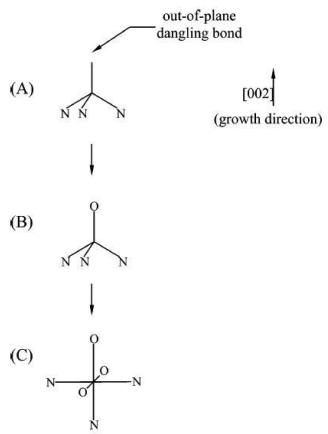

Figure {5.9}: *Schematic of the interactions of oxygen with the GaN tetrahedral structure [35].*

By modeling the measured data from VASE using EMA model we were able to extract precisely the volume of voids in as-sputtered films. For the purpose of this study the deposited layer is modeled as a mixture of GaN, Ga_2O_3 and air and the Bruggeman EMA approach was employed to derive the dielectric functions. Fitting parameters were the fractions of Ga_2O_3 and air in the layer as well as the layer thickness. As the ratio of voids in thin films increased, the trend of augmentation of relative oxygen content in films was intense leading to low refractive index values, as shown in Figure {5.10}.

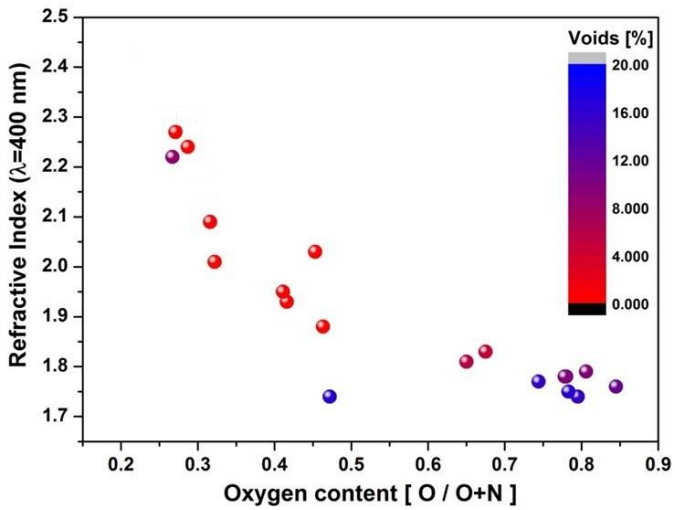

Figure {5.10}: *Plot of refractive index as a function of relative oxygen content, with relation to voids % in films (extracted from SE-EMA results).*

A SEM micrograph, showing the surface of GaN thin film (sample S1687) which is dense with smooth surface, is shown in Fig. {5.11a}. On the contrary, GaN film denoted S1678 has rougher surface with porosity having a void ratio of 0.155, extracted from EMA model, as illustrated in Fig.{5.11b}. We can deduce that there is a good correlation between SEM and SE-EMA results.

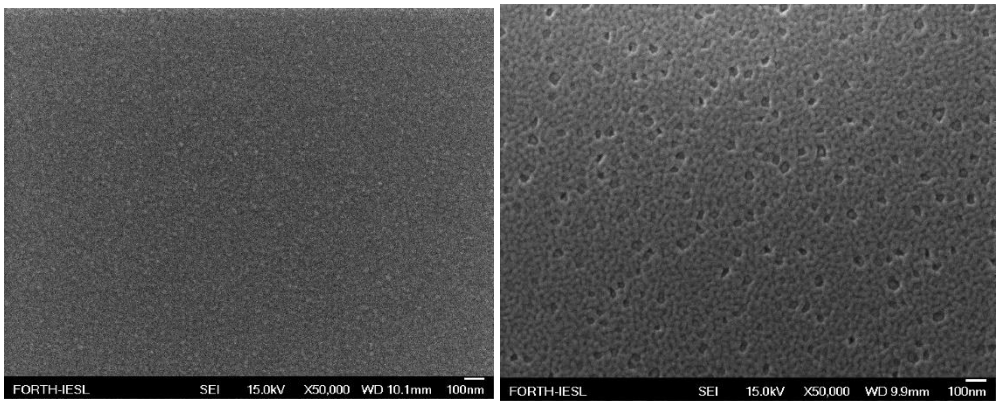

Figure {5.11}: *SEM micrographs showing a) the surface of S1687 sample and b) the surface of denoted S1678.*

In Fig. {5.12}, the measured and simulated data for the case of S1687 sample are compared to illustrate the modeling accuracy. As depicted, the experimental values (dots) and the simulated curves (continuous lines) of the ellipsometric angles Ψ and Δ are in good agreement, for 65^0, 70^0 and 75^0 angles of incidence. Since the quality of fit is high the extracted parameter values are trustworthy.

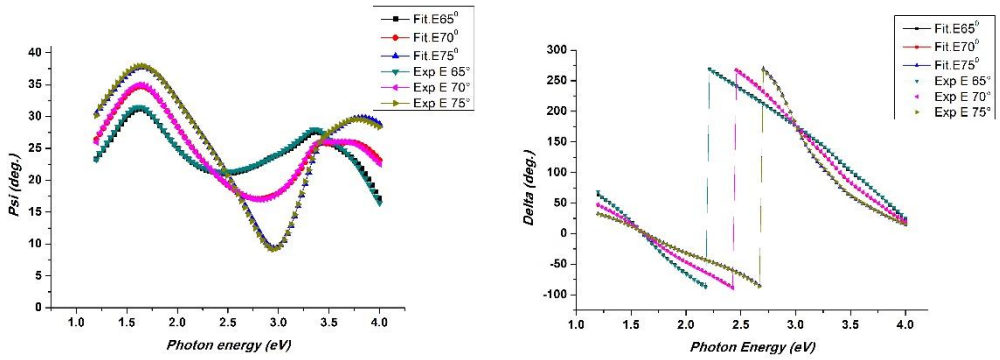

Fig. {5.12}: *Experimental Ψ and Δ vs photon energy along with the model fit.*

Hence, in the end of this series of experiments we were ready to determine the pre-cleaning conditions. Pre-sputtering for 5 hrs sinters the surface of the target slightly; then the target shows a stable operation. The pre-deposition protocol was set as follows: once the target was caused proper cleaning at 9.5 mTorr for 1 hr , nitrogen gas flow was quickly reduced and the total pressure was set to 5 mTorr for 3 hrs. The last 1 hour prior the deposition, pre-sputtering pressure was fixed at the working pressure of each growth. Last but not least, in a case that pre-cleaning was performed for less than 5 hrs, deoxidization and condensation of GaN target was not realized sufficiently.

Bandgap variation with RF Power

Initially, the dependence of the growth rate of films on the cathode target potential (or the negative DC bias) is shown in Fig. {5.13}. The deposition rate was increased almost linearly from 0.66 to 0.9 nm/min as the DC bias was raised from 1050 to 1300 V. The observed linear relationship between the two can be explained by the rise of the RF power, since DC bias V_{DC} is given by: $V_{DC} = k\frac{P_{RF}}{p}$, where P_{RF} is the RF target power and p is the working pressure and k a constant. Since the working sputtering pressure was fixed, the RF power is considered to be higher at increased cathode target potential.

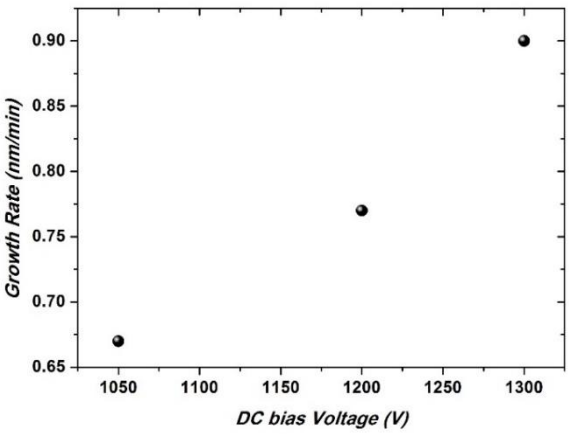

Figure {5.13}: *Dependence of DC bias voltage on growth rate for GaN thin films.*

As a consequence, the sputtering yield was increased as the RF power was raised, leading to a higher energy of incident ions onto the target. Moreover, the plasma density increases with increasing power which lead to the enhanced growth rate at higher RF powers.

The optical band gaps, plotted in Figure {5.14}, show a decreasing trend with increasing RF target power from 4.07 eV at 300 W to 3.43 eV at 500 W. The lower value is close to the bulk GaN value of 3.4 eV.

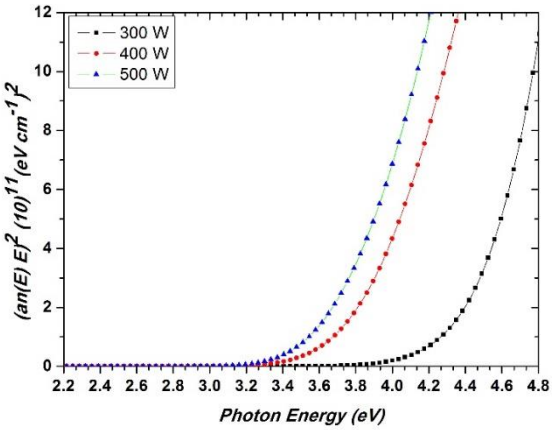

Figure {5.14}: *Plot of $(a*n*E)^2$ versus photon energy for the GaN films grown at different RF powers.*

As it was expected refractive indices show an increasing trend with increasing RF power, close to the reported values 2.35-2.60 for polycrystalline gallium nitride in particular as regards GaN film S1687 denoted, grown at 500 Watt RF power (see Fig. {5.15}).

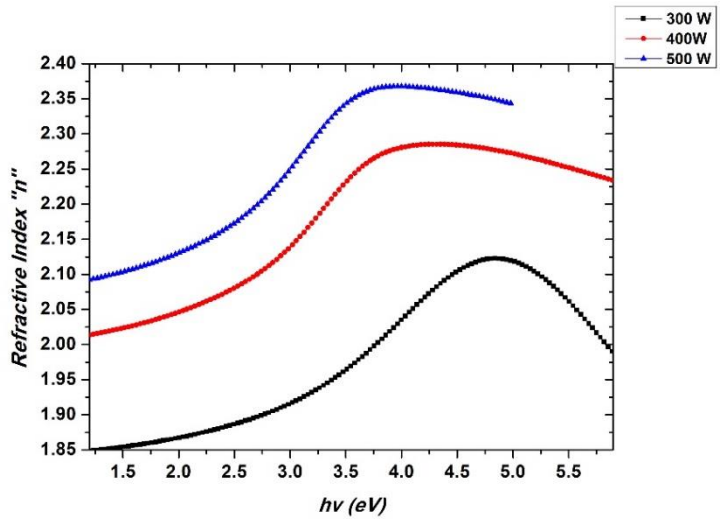

Figure {5.15}: *Typical refractive index curves for the GaN films grown at different RF powers.*

Moreover, oxygen content was reduced from 34.5 at. % for the as-sputtered film in 300 W to 23.7 at. % for the deposited film in 500 W (see Fig. {5.16}). The inverse correlation between oxygen content and film deposition rate is believed to be due to the increased time for oxygen to be incorporated into the GaN film at lower growth rates. During the residence time of the absorbed nitrogen atom, only if simultaneously a gallium atom reaches and forms a bond which traps the nitrogen atom, the nitrogen atom would be incorporated and each Ga would trap two nitrogen atoms. Another possibility is the formation of N-N bonds or O-N bonds weaker than the Ga-N bonds.

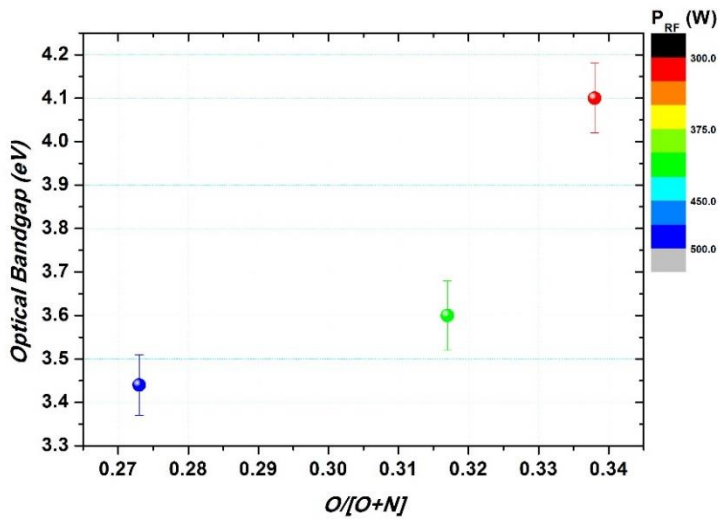

Figure {5.16}: *Plot of the optical bandgap determined from VASE measurements versus relative ratio O/[O+N] content taken from EDX data for GaN films grown at different RF powers.*

Ultimately, electrical measurements showed that GaN is too resistive to measure. Annealing at 750° C for 60 sec in a RTA-system under N_2 flow didn't significantly change the resistivity of the samples and, therefore, electrical measurements could not be performed. The resistivity of the deposited film S1687 was high, typically higher than $2*10^3$ Ω*cm and after RTA had resistivity of 1315 Ω*cm. Thus, carrier concentration and mobility values couldn't be determined due to the high resistivity of the samples.

5.1.4 Mg-Doping of GaN

The undoped GaN film is naturally n-type because of nitrogen vacancies. Hence, p-type material must relatively free of nitrogen vacancies (V_N) or contain a sufficiently large number of acceptors to compensate them. A promising p-type dopant is Mg which has emerged as the p-type dopant of choice since it exhibits a large thermal activation energy of 200 meV which results in the ionization of only a few percent of the acceptor atoms at room temperature. Thus, large concentrations of Mg are required to achieve the p-type conductivity. However, increase of Mg doping level over 10^{21} cm^{-3} deteriorates the crystal quality and surface morphology, causing a large concentration of Mg interstitials. Usually more electrons were created and higher defect densities when more Mg was added. Additionally, achieving high hole concentrations with Mg as the dopant has proved difficult. Even though it is possible to increase the Mg concentration, the hole concentration levels off and even decreases past a certain point [18]. Furthermore, the most important factor is the solubility of Mg in GaN, which is limited by competition between incorporation of Mg acceptors and formation of Mg_3N_2 [19]. Mg prefers the substitutional Ga site, and incorporation of Mg on substitutional N sites (Mg_N) or on interstitial sites (Mg_i) is unfavorable, as seen in Figure {5.17}.

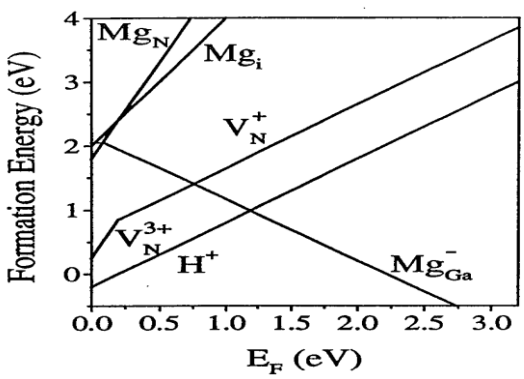

Figure {5.17}: *Formation energy as a function of Fermi energy for Mg in different configurations (the zero of Fermi energy is located at the top of the VB) [19].*

In this series of experiments, it was attempted to deposit p-type GaN films by placing Mg pellets onto the GaN target. It was thought that the trend of increasing the RF target power had to be continued, this would coincide with optimum structural properties, evidenced by narrow FWHM of the peak from XRD pattern and high degree of crystallinity. Additionally, it was anticipated that the Mg content should be adjusted through the power applied to the target along with the number of pellets onto the target.

The GaN doped samples in this project were sputtered with P_{RF} between 400 and 550 W. Initially, two pellets of Mg were placed onto the target. The samples, using values of 400 and 500 W for rf target power, gave optical bandgaps far from the value of 3.4 eV, as it is shown in Table {5.4} and relative oxygen concentration from 0.318 to 0.243 due the domination of oxides and/or oxynitride phases. As it was correctly expected the applied RF power must be increased to enhance the improvement of the as-deposited samples and to lead in higher Mg concentrations. Thus, the as-deposited film was observed with a Mg atomic percentage of~0.9% and Mg/(Mg+Ga) relative metallic ratio close to 0.03 when four Mg pellets were added onto the target.

Sample	Thickness (nm)	P_{RF} (W)	Number of Mg pellets	Dep. Rate (nm/ min)	O/ [O+N]	N/ Ga	Mg/ (Mg+Ga)	E_g (eV)
S1696	135	400	2	0.85	0.318	3.90	-	3.83±0.08
S1697	133	500	2	1.02	0.272	3.79	-	3.48±0.07
S1698	125	550	2	1.04	0.265	3.24	-	3.40±0.07
S1699	380	550	4	1.03	0.243	1.72	0.029	3.36±0.06

Table {5.4}: Growth data for GaN:Mg films grown at different sputtering conditions, relative oxygen and Mg metallic concentration in the as-sputtered films and their optical bandgaps.

The band gap of Mg-GaN films which was obtained by extrapolating the linear part of the curves of Figure {5.18}, are shown in Table {5.4}. Hence, the Mg-doping in GaN did not exhibit a large change in optical band gap.

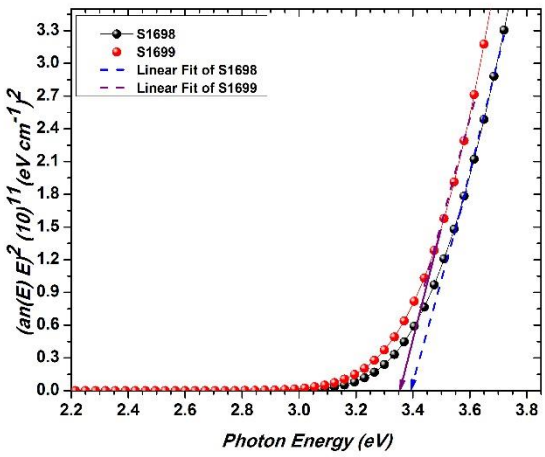

Figure {5.18}: *Plot of $(a*n*E)^2$ versus photon energy for the GaN:Mg films doped with different number of Mg pellets onto the target.*

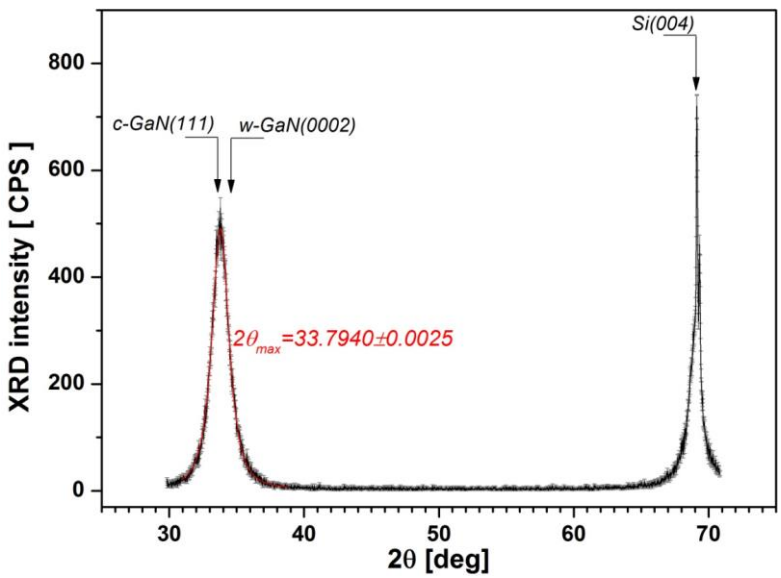

Figure {5.19}: *XRD diffraction pattern of GaN film denoted S1699.*

Figure {5.19} shows the X-ray diffraction pattern of Mg-GaN film grown on Si (100) substrate with Mg content of 2.9 at. % metallic. Mg-GaN film showed a mixed phase of cubic zinc-blende structure and hexagonal wurtzite structure, and preferentially grown along the (111) crystal plane of zinc-blende and the (0002) plane of wurtzite. No second phases had been detected, which indicated the Mg incorporation into GaN to form a solid solution or the Mg cation substituted the lattice site of the Ga cation. As we have seen in the previous section, the 2θ peak position of the undoped GaN film located at $2\theta=33.81^0$. As the Mg-doping content increased the peak position was slightly shifted to lower value of 33.79^0. The full-width at half-maximum (FWHM) of the diffraction peak of the Mg-GaN film (S1699) was 1.38 deg. and the grain size of crystallites reached about 6.1±0.1 nm. Finally, the large reflection intensity was obtained with the high level of Mg doping and the thicker film, indicating a high degree of texturization and better alignment procedure.

Annealing at 900° C for 90 sec in a RTA-system under N_2 flow didn't significantly change the resistivity of the samples and, therefore, electrical measurements could not be performed. The resistivities of the deposited films were high and are listed below.

Sample	**Mg pellets**	**ρ (Ω*cm)**	**ρ_{RTA} (Ω*cm)**	**Mg (at. %)**
S1687 (undoped)	0	>2000	1315	-
S1696	2	>2000	>2000	-
S1697	2	>2000	>2000	-
S1698	2	>2000	1731	-
S1699	4	>7600	>7600	2.9 %

Table {5.5}: *Results of resistivity obtained for the optimum undoped GaN and GaN:Mg doped samples.*

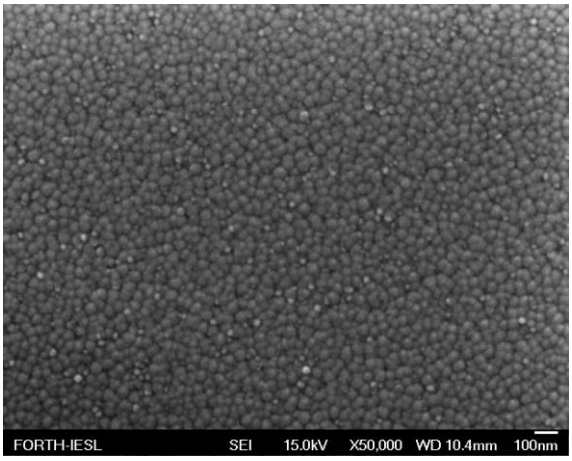

Figure {5.20}: *SEM micrograph showing the surface of denoted S1699 GaN:Mg film.*

Figure {5.20} shows SEM surface image of GaN:Mg as-sputtered thin film denoted S1699. It is clear that this film exhibit a granular surface structure, rougher than the undoped GaN thin films.

5.1.5 Alteration of the working distance

In the fourth series of experiments, the separation distance between the substrate and the target was changed from 9.9 cm to 5.5 cm. It was expected that higher deposition rates would be achieved. Thus, a higher deposition rate implied a higher productivity with a greater number of atoms/molecules arriving at the substrate in a given time. Subsequently, the substrate will get more bombardment which is favorable to the formation of the high-density films.

Reducing the target to substrate distance is a simple and direct way in order to increase deposition rate along with the power density of plasma. The sputtered particles' arrival rate varies as the inverse square of the target-to-substrate distance (see equation (7)). However, it is important to consider that the shorter separation distance affect the film uniformity. Material leaves the target in roughly a cosine distribution pattern, then the larger the separation distance the higher the number of thermalizing collisions between sputtered atoms and gas atoms. These collisions tend to flatten out the cosine distribution results in more uniform deposition across the substrate. We know from empirical data that uniformity problems start below 5 cm separation distance. Hence, in this project it is not expected to face these problems.

It can be seen that the deposition rate decreases as the target-substrate distance increases, keeping constant the sputtering pressure at 2 mTorr and target RF power at 400 W, as shown in Table {5.6}.

Sample	**$D_{sub.-tar.}$ (cm)**	**Dep. Rate (nm/min)**	**E_g (eV)**
S1685	9.9	0.77	3.59±0.07
S1700	5.5	2.87	3.57±0.07

Table {5.6}: *Growth data for GaN films grown at different working distance and their optical bandgaps.*

Figure {5.21} shows the absorption edge of the as-deposited films prepared at different target-substrate distance. It can be shown that E_g decreases as the target-substrate decreases, a fact that correlates to slightly further decrease of oxygen content in the film.

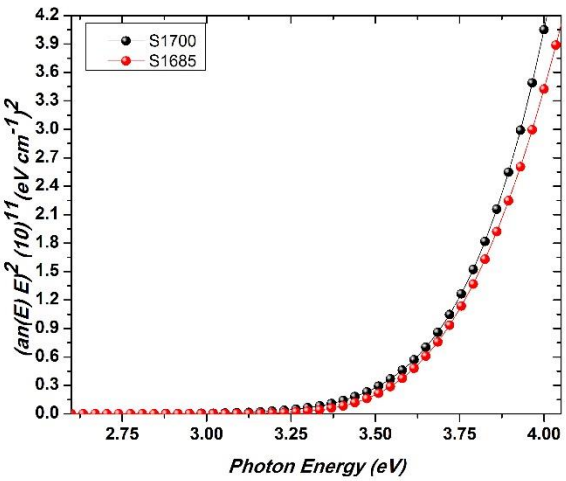

Figure {5.21}: *Plot of $(a*n*E)^2$ versus photon energy for the GaN films grown at different working distance.*

The RF power used and the working pressures are summarized in Table {5.7} along with the EDS results for oxygen concentration. Additionally, table lists the deposition rate and the optical band-gap. Therefore, it is obvious that the deposition rate is linearly proportional to the cathode RF power. Basically, the sputtering yield of the target material and the number of ions striking the target are the two factors which determine substantially the deposition rate.

As seen from the Table {5.7} the as-deposited films were improved with the RF power. Films deposited at lower power levels exhibited a poorer texture, and optical band-gap far from the value of 3.4 eV of bulk GaN. This is believed to be due to higher oxygen incorporation into the film proved by the EDX results. Furthermore, the electron density (n_e) and electron temperature (T_e) directly affected the film growth. At higher pressures, electron density increases while electron temperature decrease resulting the reduction of the excitation rate of N. Lastly, the thickness of samples was ranged from 200 up to 280 nm.

Sample	**P_{RF} (W)**	**P (mTorr)**	**V_{DC} (V)**	**O/ [O+N]**	**O (at.%)**	**Dep. Rate (nm/min)**	**E_g (eV)**	**n (at 364.7 nm)**
S1701	400	9	1200	0.453	33.73	4.77	3.78±0.08	2.07
S1702	400	4	1250	0.287	22.38	3.09	3.55±0.07	2.29
S1703	550	3.5	1450	0.284	22.09	3.94	3.48±0.07	2.35
S1704	550	4	1450	0.254	18.54	4.14	3.53±0.07	2.41
S1705	600	4.25	1500	0.283	21.09	4.91	3.55±0.07	2.36
S1706	600	5	1500	0.291	21.81	5.09	3.51±0.07	2.35
S1707	600	2.25	1550	0.229	17.45	4.15	3.41±0.06	2.46

Table {5.7}: *Growth data for GaN films grown at different sputtering pressure, their optical bandgaps and refractive indices from SE and their oxygen content taken from EDS.*

From Figure {5.22}, we can conclude that optical bandgaps show a decreasing trend with lower O/[O+N] ratio which can be controlled by decreasing the sputtering pressure from 9 mTorr to 2.25 mTorr.

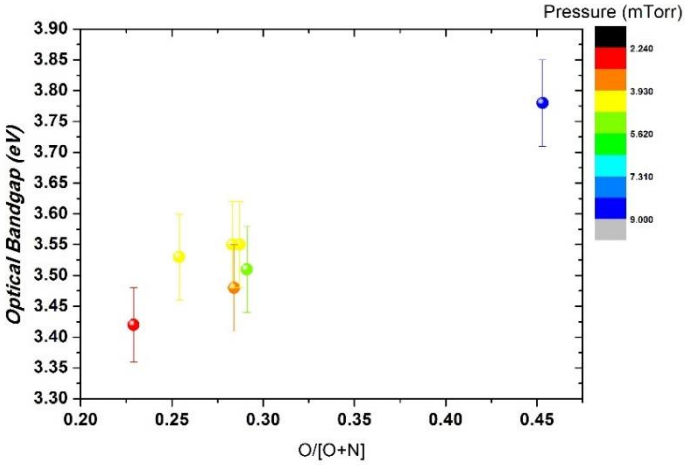

Figure {5.22}: *Plot of optical bandgap versus relative oxygen content for the GaN films grown at different sputtering pressure.*

Furthermore, it is imperative to point out that effects of gas pressure during the deposition are similar to previous case with increased target-to-substrate separation. Hence, the increased growth rate results in rise of relative oxygen content in GaN thin films, as illustrated in Figure {5.23}. So, the influences of the RF power and sputtering pressure are opposed. The beneficial effects of ion bombardment include the increase of surface mobility of adsorbed reactive species. These indications enhance the argument that as the plasma is more ‘’confined’’ the oxygen concentration in films is decreased. Therefore, a possible explanation could be that in low pressure the projectile ions have higher energy due to less thermal collisions with atoms. This may increase the ratio of sputter atoms from target grains core to grains oxidized surface. So, these results suggest that when the incident ion energy increases, energy losses in the target also increase such that the energy of incident ions is not effectively transferred to sputtered atoms, thus reduce the growth rate.

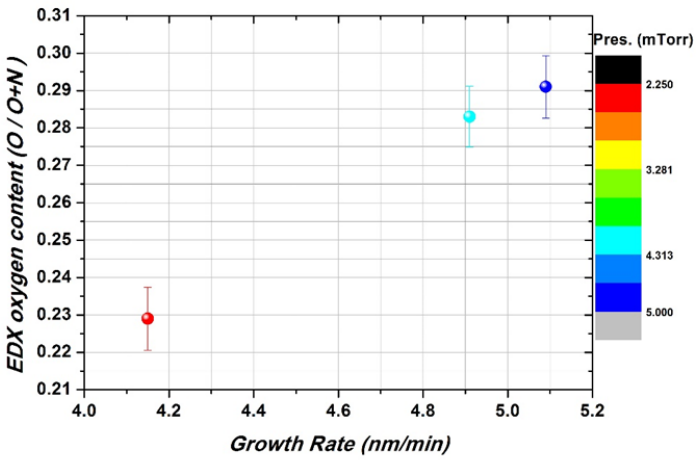

Figure {5.23}: *Plot of relative oxygen content versus growth rate for the GaN films grown at different sputtering pressure and at 600 W RF power.*

There are several nitrogen species which are expected to be present in the discharge and can be chemisorbed. Atomic nitrogen impacting the growing film should be readily chemisorbed. N_2^+ ions with energies > 9 eV (dissociation energy of nitrogen is 8.7 eV) have a high probability of dissociating upon impact with the film surface to form two free nitrogen atoms. Higher-energy particles >75 eV are incorporated in the film by embedding themselves in the lattice [37]. Additionally, there are several mechanisms by which the various sorbable nitrogen species can reach the film surface with the appropriate energies. It is known that a dc self-bias develops on the target (V_{DC}) ,which is negative with respect to ground, since electrons are substantially more mobile than ions at the RF frequency of 13.56 MHz. The plasma assumes a positive potential {V_p} with respect to ground for most of the rf cycle and the potential drop across the cathode dark space is (V_p- V_{DC}) which represents the maximum energy of accelerated ions can have available, across the dark space, for sputtering.

Here we have to mention that the trend of growing nitrogen rich films at low pressure continued. The mean free path in the gas phase was at a maximum so that the neutrals reflected from the target will have the maximum probability of arriving at the substrate with a substantial fraction of their initial energy. The target self-DC-bias was expected to be weakly dependent on pressure, keeping fixed the target power. This is consistent with the experimental results since the DC bias dropt only slightly with sputtering pressure (≈ 4% decrease in going from 4 to 9 mTorr). At the same time the mean free path decreases which implies the reflected energetic neutrals undergo more frequent energy dissipating collisions until the species reach the substrate. Therefore, fewer of them are able to reach the film surface with sufficient energy to be incorporated. However, it was observed that the deposition rate was increased as the sputtering pressure increased because energy dissipating collisions produce a number of new energetic particles like oxygen. Thus, oxygen contents were getting high in as-deposited thin films when nitrogen gas pressure was increased.

Moreover, the films became less nitrogen rich as the N_2 pressure in the discharge was increased. Qualitatively, this feature can be understood by considering the effect of pressure on the rate of impingement of gallium and active nitrogen species on the substrate. A tendency for films to be strongly nitrogen rich at the lowest pressure is attributed mainly to incorporation of energetic neutrals reflected from the target or probably to increased excited nitrogen plasma species reaching substrate.

We concluded that the process pressure and the RF power can be regarded as the parameters responsible for the dramatic improvement in the texture and the optical properties of thin films. Taking into account the optical band gap and the oxygen content of films, we found that the 600 RF target power at 2.25 mTorr sputtering pressure gave the best properties.

Fig. {5.24} shows the optical constants, *n* and *k*, for sample S1707 grown under optimum deposition conditions. The refractive index *n* varied from 2.15 to 2.48 in the range of 210-1040 nm, with maximum occurring at about 330 nm. The extinction coefficient *k* varies smoothly and above the wavelength 460 nm, *k* equals to zero indicating that the film is transparent in this region.

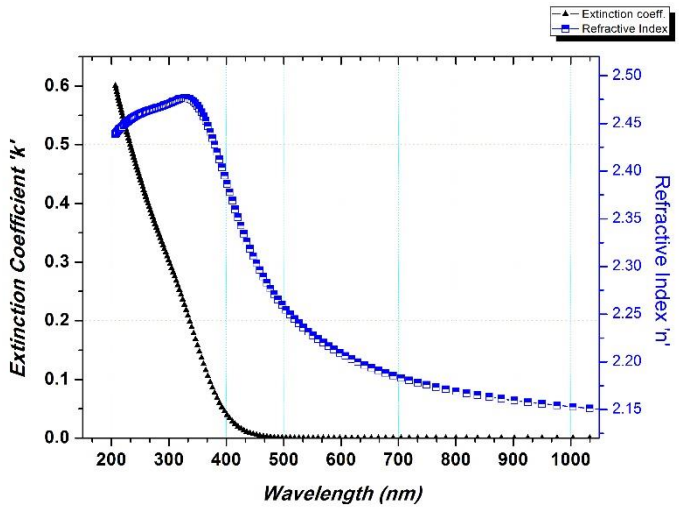

Figure {5.24}: *Plot of relative oxygen content versus growth rate for the GaN films grown at different sputtering pressure and at 600 W RF power.*

Figure {5.25} illustrates the x-ray diffraction 2θ/θ scan of the GaN film grown at RF cathode target power of 600 W at 2.25 mTorr sputtering pressure. A single Bragg diffraction peak is observed at 33.98^0, which is attributed to a mixed phase of zinc-blende and wurtzite GaN. The full-width at half maximum (FWHM) of this reflection was measured to be 1.98^0. Finally, the crystallite size estimated at 4.2±0.1 nm.

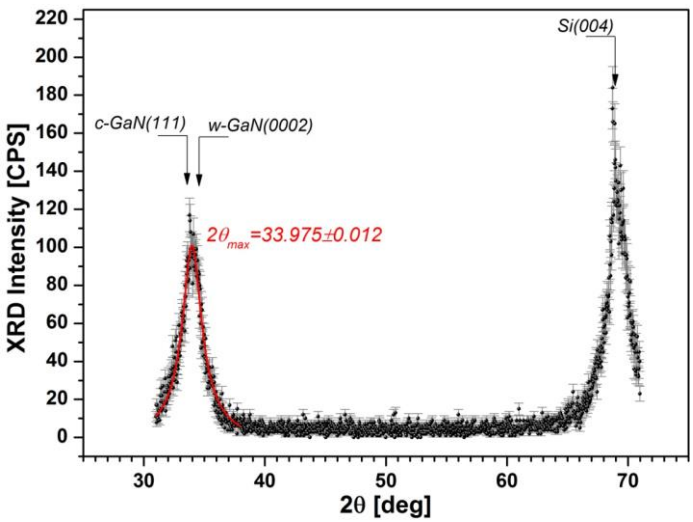

Figure {5.25}: *XRD diffraction pattern of GaN film denoted S1699.*

The XRD diffraction patterns of GaN films denoted S1707 and S1687 are shown in figure {5.26}. Generally, the thermodynamically stable structure for GaN is wurtzite. Reducing target-substrate distance the nitrogen plasma became more ‘’concentrated’’ and the species more energetic arriving at the substrate. It is easily observable the slight sift of peak towards wurtzite GaN lattice constant when the separation distance of target to substrate decreased from 9.9 cm to 5.5 cm.

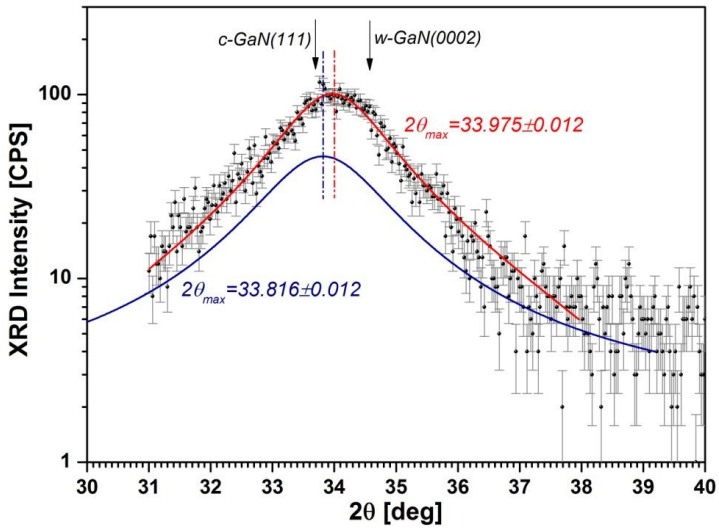

Figure {5.26}: *XRD diffraction pattern of GaN film denoted S1707 compared to S1687.*

Figure {5.27} shows SEM surface images of GaN as-sputtered thin films grown at different RF power and sputtering pressure. We notice that there is a strong correlation of surface morphology of thin films to gas pressure and the thin film grown at low pressure of 2.25 mTorr and RF power of 600 Watt exhibit the smoothest surface.

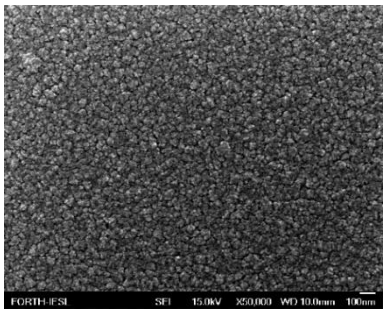

Figure {5.27}: *SEM micrographs showing a) the surface of S1701 sample grown at 9 mTorr and 400 W*

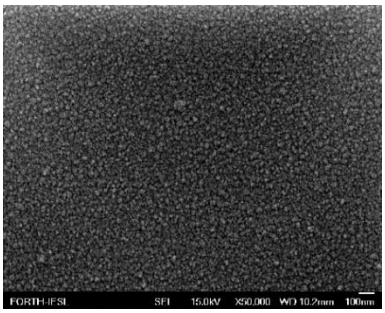

b) the surface of S1706 sample grown at 5 mTorr and 600 W

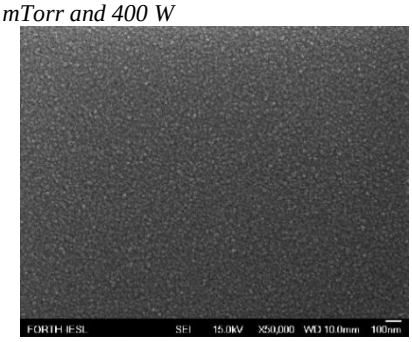

c) the surface of S1705 sample grown at 4.25 mTorr and 600 W

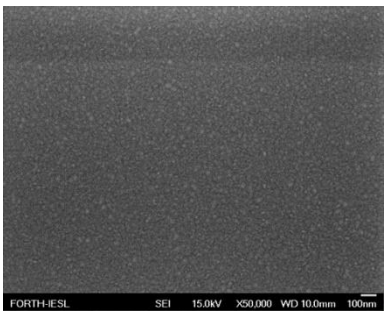

d) the surface of S1707 sample grown at 2.25 mTorr and 600 W

5.2 Sputtering InGaN

5.2.1 Experimental Approach

In the last series of experiments, it was attempted to deposit InGaN films by placing In pellets onto the GaN target. It was expected that the resistivity of as-deposited InGaN thin films would be decreased with increasing In content [38]. Additionally, the indium content was adjusted through the number of pellets onto the target and of course through the RF power applied to the target (or the DC-self-bias V_{DC}). These parameters changed in this study are summarized in Table {5.8} maintaining a constant sputtering pressure of 2.25 mTorr for all samples grown. Samples are made at RF powers of 550 W,600 W and 650 W. Moreover, the thicknesses and the deposition rates of the deposited films can be found also in Table {5.8}. It is widely known that the sputtering yield, at Ar^+ incident, of indium is much higher than the yield of Ga [31]. However, during the plasma of only nitrogen atmosphere, maximum energy transfer function during elastic collision between target atom and projectile ion (N^+ or N_2^+), from equation (1), is given by

$$\gamma = \frac{4M_1M_2}{(M_1 + M_2)^2}$$

where M_2 the atomic mass of the target atom with zero initial energy and M_1 the atomic mass of nitrogen projectile ion. So, from the above equation $\gamma_{Ga\text{-}N}^+=0.56$ and $\gamma_{In\text{-}N}^+=0.39$ which implies the sputter yield for gallium is higher than indium during nitrogen ion bombardment.

It is imperative to say that the flux of indium sputtered species was strongly directional since the place geometry of indium pellets onto the target was the project of it on the substrate. Visual observations showed that the holder of the samples was always colored brown after each run, forming an enlarged shape of each pellet. In Table {5.8}, it can be seen that with further increase of indium pellets from six to ten, the deposition rate rapidly increased. Furthermore, as it was expected the deposition rate tends to increase with increasing RF power. An approximation of the resulting Indium in the film was given by EDS.

Sample	Number of In pellets	Dep. Rate (nm/min)	Thickness (nm)
S1711	6	4.45	489
S1712	6	5.13	487
S1713	6	5.20	390
S1715	10	6.71	772

Table {5.8}: Deposition rate and thickness of InGaN films grown at different RF power and with different number of indium pellets.

5.2.2 Bandgap tuning with RF power and In pellets

Optical bandgap tuning by varying RF power and the number of Indium pellets onto the target is explained in this subsection below.

Sample	Number of In pellets	Power (Watt)	O (at.%)	O/ [O+N]	In/ (In+Ga)
S1711	6	550	13.83	0.211	0.171
S1712	6	600	12.08	0.185	0.178
S1713	6	650	12.49	0.184	0.179
S1715	10	650	13.01	0.209	0.302

Table {5.9}: Growth data and EDS results of InGaN films grown at various RF power and number of indium pellets.

As it can be observed from Table {5.9}, it is clear that the indium atomic composition increases with the increase of the RF power and the added indium pellets onto the target.

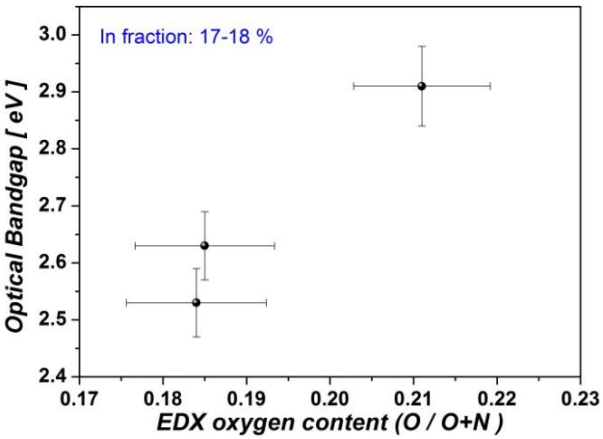

Figure {5.28}: *Optical bandgap versus relative oxygen content for the InGaN alloys grown at the same number (6) of indium pellets.*

Furthermore, the tendency of proportional dependence between the optical bandgap and the ratio of O/[O+N] remains powerful, as depicted in Fig. {5.28}.

The existence of oxygen indicates that as-deposited films are indeed mixed phase of InGaN, In_2O_3, Ga_2O_3 and/or indium oxynitride phases. Although, the atomic percentage of oxygen in InGaN sputtered films was lower than that of GaN sputtered films. This may have contributed to the drop of resistivity of InGaN thin films compared to high resistivity of GaN as-deposited films. X-ray diffraction patterns revealed that the films grown on the substrates were amorphous.

The results indicate that the sputtering yield of indium was augmented with the increasing of RF power since the ions gain more energy attracted from the increased self-DC bias voltage of target. Hence, the higher incident energy of ions sputters more indium atoms and thereby decreases the bandgap of InGaN thin films (see Fig. {5.29}).

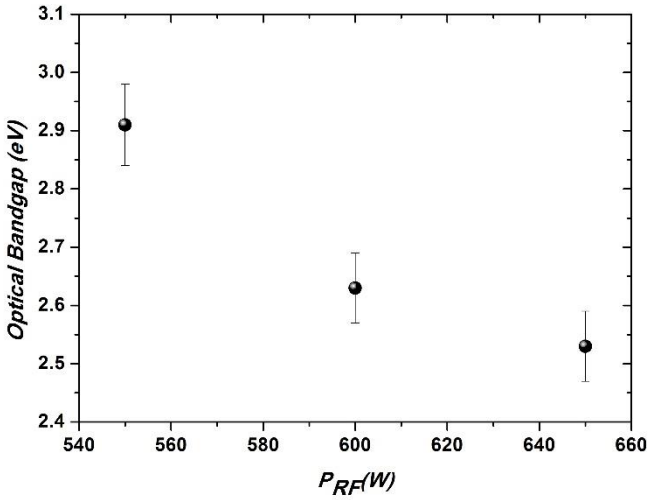

Figure {5.29}: *Optical bandgap versus RF power for InGaN films grown at the same number (6) of indium pellets.*

The calculated refractive index spectra determined for the In content *x*=In/[In+Ga]=0.171, 0.178, 0.179 and 0.302 are plotted in the photon energy range of 1.5-3.2 e V in Fig. {5.30}. From figure {5.31}, it is clear that the optical bandgap widens with the increasing of indium incorporation in InGaN films. This reflects the change of indium content with the change in the RF power and proves the solubility between InN and GaN.

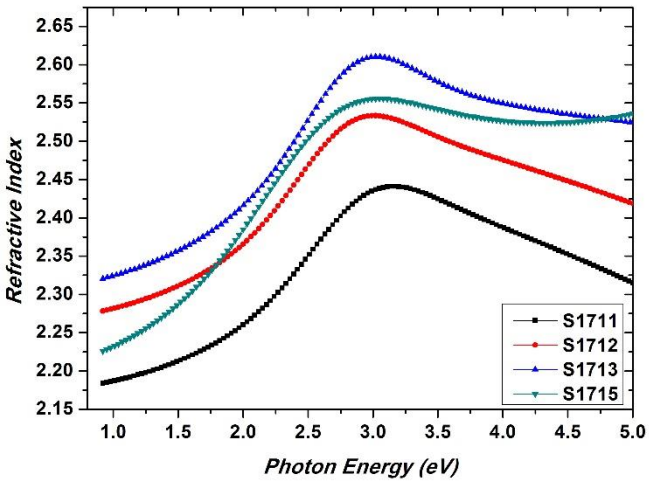

Figure {5.30}: *Typical refractive index curves for the InGaN alloys.*

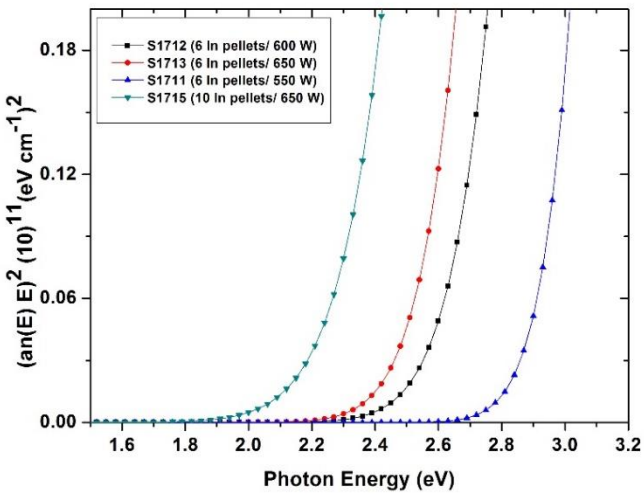

Figure {5.31}: *$(a*n*E)^2$ as a function of photon energy for the grown InGaN alloys with various In content.*

In Table {5.10} are listed the number of Indium pellets placed onto the target, the self-DC bias of target and the calculated optical bandgaps for each alloy.

Sample	Number of In pellets	V_{DC} (V)	E_g (eV)
S1711	6	1450	2.91±0.07
S1712	6	1500	2.63±0.06
S1713	6	1600	2.53±0.06
S1715	10	1600	2.15±0.05

Table {5.10}: The optical bandgap of InGaN films grown at various RF power and number of indium pellets.

5.2.3 Mg-Doping of InGaN

P-type doping in InGaN alloys, especially in relatively high In content, is highly challenging due to the presence of high background electron concentrations, which is believed to originate from defects such as oxygen or nitrogen vacancies and hydrogen impurities [41]. The latter is absent from our chamber since the sputtering method didn't use metalorganic species and hydrogen atmosphere preventing the formation of Mg-H bonding. Furthermore, Kumakura et al. and B. N. Pantha et al. reported that the activation energy for Mg-doped InGaN decreased with an indium mole fraction increase (or a bandgap energy decrease), as illustrated in Fig. {5.32} [39,40]. In order to achieve p-type conductivity we followed this concept by increasing the number of pellets onto the target.

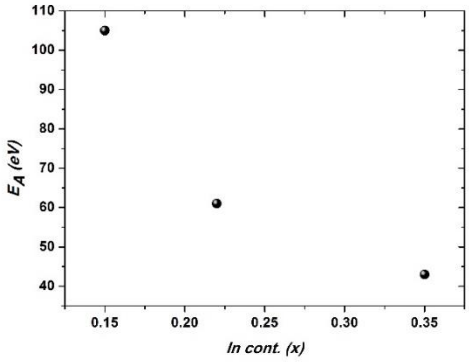

Fig. {5.32}: *Data from reference [40]. Energy level (E_A) of Mg acceptors in Mg doped $In_xGa_{1-x}N$ alloys as a function of In content x.*

Hence, the InGaN Mg-doped samples were sputtered maintaining a constant sputtering pressure of 2.25 mTorr and P_{RF} of 650 W. The parameters changed in this section, such as number of pellets, along with the EDX results and the deposition rates of the deposited films are summarized in Table {5.11}. Moreover, the thickness of samples was ranged from 630 up to 670 nm.

Sample	Number of In pellets	Number of Mg pellets	Dep. Rate (nm/min)	O (at.%)	O/ [O+N]	In/ (In+Ga)	Mg/ (In+Ga+Mg)
S1714	6	3	5.61	14.53	0.231	0.185	0.014
S1716	7	6	5.62	14.02	0.223	0.248	0.062
S1717	7	10	5.27	12.56	0.201	0.236	0.115

Table {5.11}: Growth data and EDS results of InGaN:Mg alloys grown at various number of In and Mg pellets.

The band-gap of Mg-InGaN films can be obtained directly by plotting the curves as shown in Fig. {5.33} and followed by extrapolating the linear part of curves. The obtained E_{gap} values were 2.61±0.06 e V, 2.52±0.05 e V and 2.44±0.05 e V for S1714, S1716 and S1717 samples respectively. Moreover, the change in bandgap was 80 meV for Mg-InGaN films with Mg content increasing from 6.2 at. % to 11.5 at. % metallic. This result seems to agree with the assumption that Mg doping doesn't significantly affect the bandgap value due to its acceptor level being 0.1-0.17 e V above the valence band maximum [42].

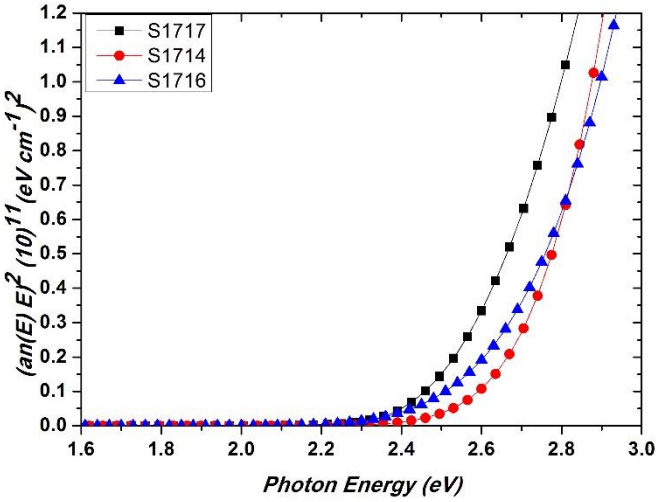

Figure {5.33}: *Plot of $(a*n*E)^2$ versus photon energy for the InGaN:Mg alloys grown at various number of In and Mg pellets.*

As it is illustrated in Fig. {5.34} the optical bandgap decreases with the drop of O/[O+N] ratio.

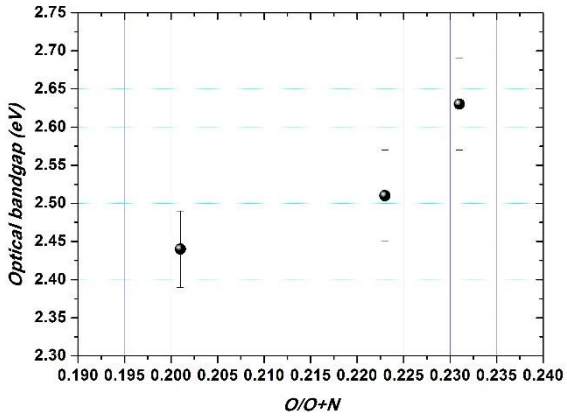

Figure {5.34}: *Plot of optical bandgap versus relative oxygen content for the InGaN:Mg alloys grown at various number of In and Mg pellets.*

Figure {5.35} shows SEM surface images and AFM morphologies of InGaN and InGaN:Mg alloys. The heavily doped InGaN:Mg alloy denoted S1717 exhibited improved surface morphology in comparison with S1714 sample which had lower magnesium metallic at. % content. Moreover, the root-mean-square (rms) roughness of S1717 sample was 1.162 nm. With the decrease in the Mg-doping content, the rms roughness of S1714 sample slightly increased to 1.794 nm. The undoped InGaN alloy denoted S1715 with 0.3 InN mole fraction had rms roughness of 2.635 nm. So, the increase in Mg doping led to more smooth surface and lower rms roughness.

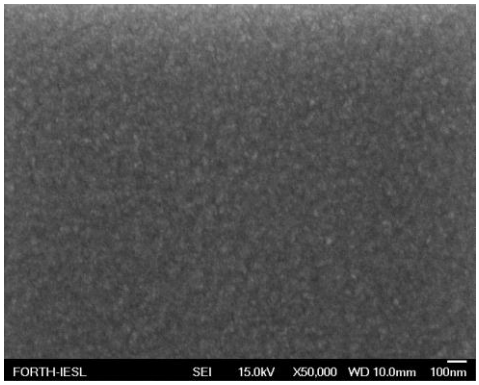

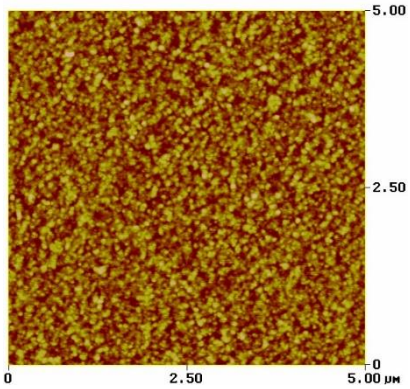

Figure {5.35}: *SEM micrograph showing*
a) the surface of InGaN:Mg alloy S1714 sample
b) AFM micrograph of InGaN:Mg alloy S1714 sample

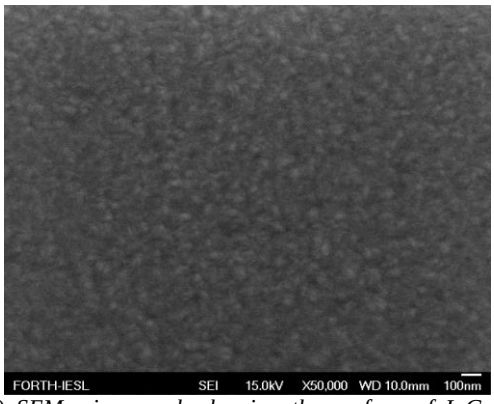

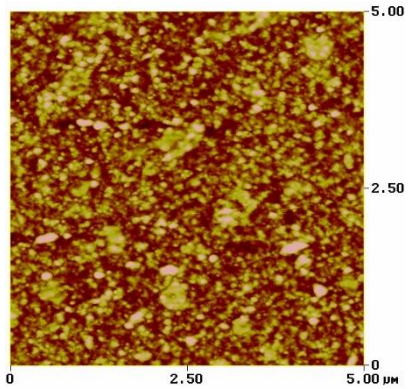

c) SEM micrograph showing the surface of InGaN alloy S1715 sample
d) AFM micrograph of InGaN alloy S1715 sample

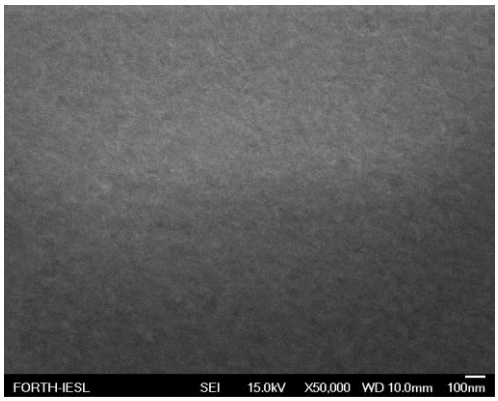

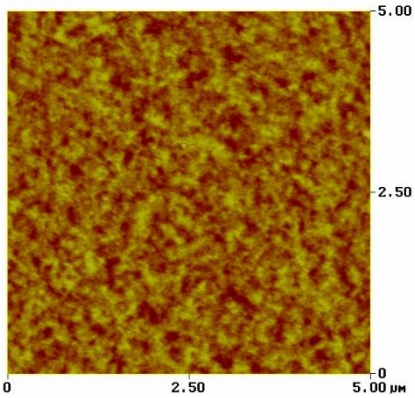

e) SEM micrograph showing the surface of InGaN:Mg alloy S1717 sample
f) AFM micrograph of InGaN:Mg alloy S1717 sample

Figure {5.36} shows the behavior of optical bandgap as a function of relative indium content (metallic at. %). The optical bandgap approaches the InGaN bandgap when the relative oxygen content is low in the as-sputtered alloys (the corresponding linear behavior of w-InGaN bandgap as a function of InN mole fraction is indicated by the blue dashed line).

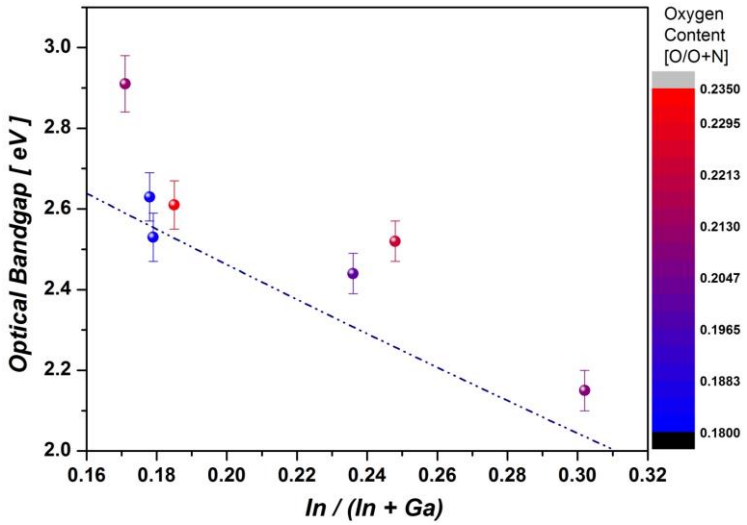

Figure {5.36}: *Plot of the optical bandgap determined from VASE measurements versus relative ratio In/[In+Ga] content taken from EDX data for as-deposited InGaN and InGaN:Mg alloys.*

5.2.4 Electrical Properties of InGaN and Mg- InGaN films

The electrical properties of as-sputtered InGaN and Mg-doped InGaN were evaluated through Hall-effect measurements. Initially, the mixture of InN with GaN shows that previously semi-insulating GaN can be made conductive over the measured compositional range. The electron effective mass of InN is smaller than that of GaN, therefore the mobility of the films increases when the In content is increased. The carrier concentrations along with the mobility were augmented by increasing InN MF for n- type undoped InGaN, which is strongly related to the increased In incorporation into InGaN, as shown in Figure {5.37} and {5.38}. Generally, the reduction in hole concentration values observed in p-type InGaN are due to the effect of hole compensation by background electrons [40]. The presence of high back background electron concentration is the main hindrance for obtaining p-type conductivity.

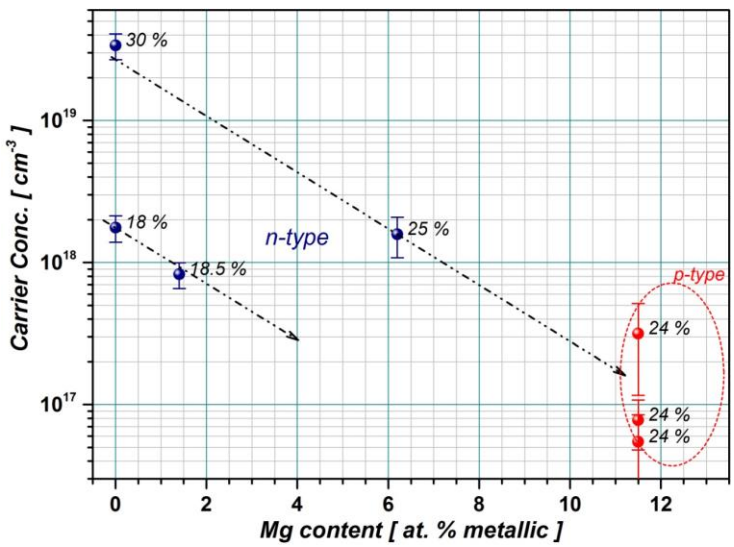

Figure {5.37}: *The carrier concentration as a function of Mg metallic at. % for as-deposited InGaN and InGaN:Mg alloys.*

It is well known that the acceptor candidate is an isolated Mg atom in the M site (Mg_B) (where M: Ga or In). The n-to-p transition supports the solid solutioning of Mg^{2+} dopant into the B^{3+} site. If Mg^{2+} doesn't substitute the B^{3+} site, it will behave as an impurity and precipitate at the grain boundary and form Mg_3N_2. Hall effect measurements showed that when the Mg dopant molar content in $In_{0.24}Ga_{0.76}N$ increased to y=0.115 (y=Mg/[In+Ga+Mg] metallic content) the as-sputtered film transformed into p-type conduction. This as-grown film transformed into p-type conduction and showed hole concentration of $5.47*10^{16}$ cm^{-3}, $7.79*10^{16}$ cm^{-3} and $3.16*10^{17}$ cm^{-3} for the three different areas of the sample.

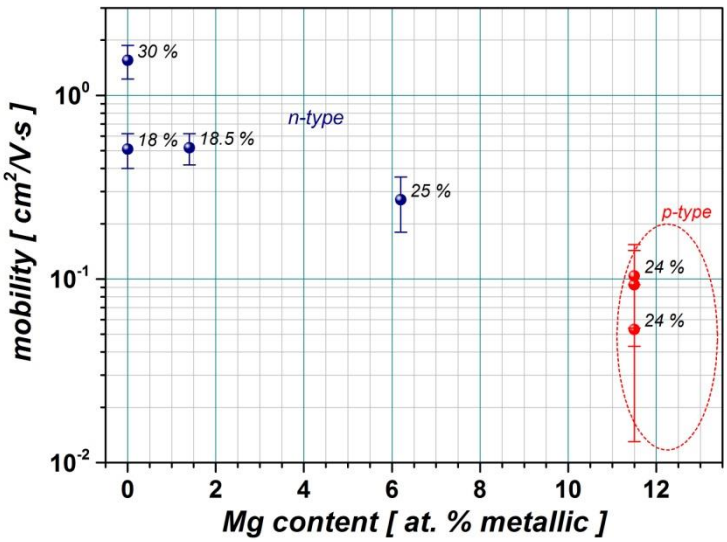

Figure {5.38}: *The mobility of carriers as a function of Mg metallic at. % for as-deposited InGaN and InGaN:Mg alloys.*

The mobility decreased to 0.093 cm^2/Vs, 0.104 cm^2/Vs and 0.053 cm^2/Vs compared to the sample with less Mg dopant molar percentage y=0.062 which had mobility 0.27 cm^2/Vs, as illustrated in Fig. {5.38}. Generally, the mobility decreases due to scattering at crystal defects or domination of ionized impurity scattering. The low mobility values are mainly due to the

low temperature in the RF sputtering process. Low temperature introduces a considerable amount of structural defects in the lattice, which in turn leads to residue imperfection scattering having as a consequence the reduction of mobility values. Finally, low growth temperature of InGaN alloys seems to promote the incorporation of donor like defects and impurities.
The carrier concentration dropped with increasing doping from y=6.2 metallic at. % of Mg to y=11.5. This decrease in carrier concentration is certainly due to the doping efficiency of Mg which is typically nearly the range of 0.1 %, limited to solubility of magnesium in the solid phase and self-compensation by V_N or other donor type defects (like oxygen).

Moreover, resistivity values were decreased in the order of 10^2 by increasing the In/[In+Ga] to 0.3 (or by increasing the number of pellets onto the target). As it is illustrated in Fig. {5.39} the variation in resistivity with y shows that ρ increases as magnesium doping increases and has a minimum value of 0.14 Ω cm at y=0. Resistivity increases with Mg content due to decrease in electron concentration.

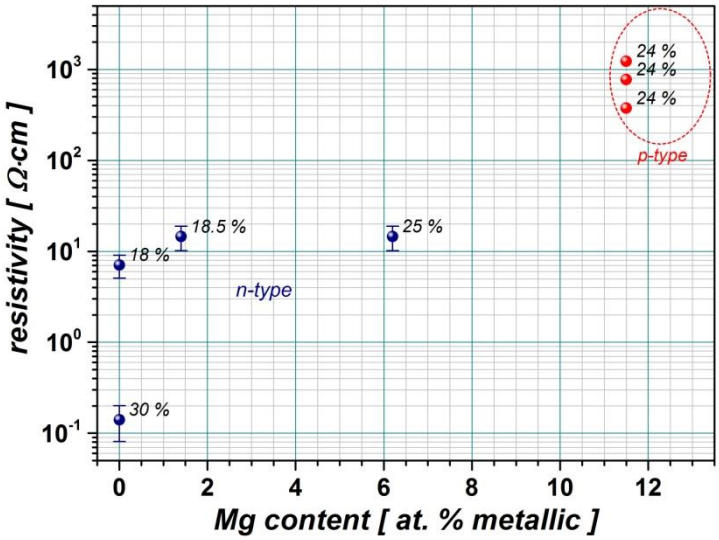

Figure {5.39}: *Plot of the resistivity versus Mg metallic at. % for as-deposited InGaN and InGaN:Mg alloys.*

We have to point out that resistivity was increased from 7.09 Ω*cm to 14.56 Ω*cm when Mg dopants were added since the precipitates surround the grain boundaries and retard the carrier concentration but the film still remained as n-type semiconductor.

CHAPTER 6

Conclusions

RF sputtering of GaN and InGaN thin films was performed on Si and fused silica substrates. Among the thin film deposition methods, sputtering has been the least studied as far as the growth of InGaN alloys. The investigations basically dealt with the growth and properties of InGaN and GaN thin films. The sputtering parameters, specifically the RF target power, sputtering pressure and the distance target-to-substrate were varied in order to optimize the structural and optical properties of the resulting films. We found that by far the most important factors are the arrival energy of the sputtered atoms, which is primarily controlled by the sputtering pressure, and the proper long hour pre-cleaning of target. Generally, the film quality increased with RF power. An optimum combination was achieved as far as the growth conditions, with the best undoped GaN film exhibiting a high degree of crystallization. Specifically, we noticed that the GaN films exhibited a mixed phase of h-GaN and c-GaN. GaN films grown at higher RF power exhibited better crystallinity. Moreover, oxygen impurities were incorporated during film growth at concentrations which affected optical and structural properties of thin films. The problem of oxygen contamination addressed sufficiently, thus GaN films with low oxide phase were obtained with smooth surfaces, reaching an optical bandgap of 3.4 e V. It is imperative to point out that the most important factor was the low sputtering pressure decreasing the growth rate along with the pure nitrogen atmosphere in plasma.

The InGaN growth was performed by RF sputtering with indium pellets onto the target. Initially, the RF power applied to the target was varied, keeping all other sputtering conditions fixed in order to obtain films with a range of indium contents in InGaN alloy. Subsequently, the number of indium pellets was augmented to reach a 0.3 InN mole fraction with low resistivity of 0.14 Ω cm and carrier concentration of $3.38*10^{19}$ cm^{-3}. We report for the first time that amorphous highly doped InGaN:Mg films can be grown at room temperature indicating a p-type conductivity. Hall effects measurements showed hole concentration of $5.47*10^{16}$ cm^{-3} up to $3.16*10^{17}$ cm^{-3} and the high doping concentration led to decreasing mobility. The optical analysis revealed an approach of optical bandgap of as-sputtered InGaN alloys to h-InGaN values, especially for low oxygen content. Last but not least, further work is necessary to try to decrease the resistivity of thin films and this would shed the light on the electrical properties of thin films.

Finally, having troubleshooted the basics of InGaN and GaN deposition by sputtering method, there are many possibilities opening for future investigations. The investigation of inserting a AlN nucleation layer can be done which could not be handled in this work. Further improvements can be made by changing the substrate temperature in order to ameliorate the material quality. The next challenge concerns the device realization by sputtering deposition of

p-n junctions. The last direction of future research should deal with the increase of indium content in alloys by adding a small portion of sputtering argon gas to plasma.

Bibliography

[1] J. Wu, J. Appl. Phys. 106, 011101 (2009)

[2] V.Y. Davydov et al., Phys. Status Solidi B 234, 787 (2002)

[3] F. K. Yam, Z. Hassan, Science Direct, Superlattices and Microstructures 43, 1-23 (2008)

[4] Takayuki et al, Journal of Applied Physics, Vol. 89,12 (2001)

[5] E. C. Knox-Davies et al., Journal of Applied Phys 99, 073503 (2006)

[6] Cheng-Che Li et al., Journal of Electronic Materials, Vol. 42, No. 8, 2013

[7] S. A. Campbell, The Oxford Series in El. and Comp. Eng. Oxford University Press, 3rd edition, 2008

[8] M.W. Thompson, Philos. Mag. 18, 377 (1968)

[9] Y. Yamamura et al, Kakuyugokenkyu 66/3 222, 277 (1991)

[10] Reactive Sputter Deposition, Diederik Depla, Stijn Mahieu, Springer, 2007

[11] Springer Handbook of Electronic and Photonic Materials, Safa Kasap, Peter Capper, Springer Science, 2006

[12] C. Kittel and P. McEuen, Introduction to Solid State Physics, Wiley New York, 8th edition, 2005

[13] S.A. Kazazis, E. Papadomanolaki, M. Androulidaki, K. Tsagaraki, A. Kostopoulos, E. Aperathitis, E. Iliopoulos, Thin Solid Films 611,46-51, (2016)

[14] Y.Zhao, C.W. Tu, I.-T. Bae, and T.-Y. Seong, Appl. Phys. Lett. 74, 3182 (1999)

[15] M. M. Shahin, Bull. Am. Phys. 11 (1966) 506

[16] Optoelectronic Devices: III-Nitrides, M. Razeghi and M. Henini, 2004 Elsevier Ltd.

[17] Chen Z, Donnelly V M, Economou D J, Chen L, Funk M and Sundararajan R 2009 J. Vac. Sci. Technol. A27 1159

[18] D. P. Bour et al {Mater. Res. Soc. Symp. Proc vol.449 (1997) p.509}

[19] J. Neugebauer , C. G. Van der Walle {Mater. Res. Soc. Symp. Vol.395 (1996) p.645}

[20] Sproul, W. D. and Tomashek, J. 1983 CA1198084A1

[21] Piner E. L., Mclntosh F. G. et al., 1996 MRS Internet J. Nitride Semicond. Res. 1-43

[22] Guide to Using WVASE Spectroscopic Ellipsometry Data, Acquisition and Analysis Software, J.A. Woollam Co., Inc. (2012)

[23] P. Ruterana, M. Albrecht, J. Neugebaue, Nitride Semiconductors, Wiley-VCH 2003

[24] http://www.physics.csbsju.edu/370/jcalvert/dischg.htm.html

[25] https://application.wiley-vch.de/books/sample/3527408371_c01.pdf

[26] O Ambacher, Growth and applications of Group III-nitrides, J. Phys. D: Appl. Phys. 31 (1998) 2653-2710

[27] http://www.mee-inc.com/hamm/energy-dispersive-x-ray-spectroscopyeds/

[28] Manual of Nordiko Sputtering

[29] https://tel.archives-ouvertes.fr/tel-01159686/document

[30] Sputtering by Particle Bombardment I, R. Behrisch, Springer-Verlag Berlin Heidelberg New York 1981

[31] Seah M P, Clifford C A, Green F M and Gilmore I S 2005 Surf. Interface An. 37 444–58

[32] Low Pressure Plasmas and Microstructure Technology, Gerhard Franz, Springer 2009

[33] G. F. Iriarte et al.: Reactive sputter deposition of highly oriented AlN films at room temperature, J. Mater. Res., Vol. 17, No. 6, 2002

[34] Semiconductor Material and device characterization, 3rd edition, John Wiley (2006)

[35] Nguyen H. Tran et al., J. Phys. Chem. B 2005, 109, 18348-18351

[36] M. D. Schofield (2011) ZnO Deposited by Magnetron Sputtering Incorporating Si and Nanocrystals (Master's thesis, University of Oslo)

[37] C. J. Mogab and E. Lugugijo , J. Appl. Phys. , Vol. 47 ,No. 4, 1976

[38] Y. Sato et al./ Journal of Crystal Growth 189/190, (1998), 42-46

[39] Kumakura K. et al, Jpn J Appl Phys Part 2, 39: L337 (2000)

[40] B. N. Pantha et al, App. Physics Letters 95, 261904 (2009)

[41] J. W. L. Yim, R. E. Jones, K. M. Yu, J. W. Ager III, W. Walukiewicz, W. J. Schaff, and J. Wu, Phys. Rev. B 76, 041303® (2007)

[42] K. Kumakura et al., J. Appl. Phys. 93, 3370 (2003)

[43] K. S. A. Butcher, H. Timmers, Afifuddin, Patrick P.-T. Chen, T. D. M. Weijers, E. M. Goldys, T. L. Tansley, R. G. Elliman, and J. A. Freitas Jr., J. Appl. Phys. 92, 3397 (2002)

[44] Jorg Neugebauer and Chris G. Van de Walle, Native defects and impurities in GaN, https://mrlweb.mrl.ucsb.edu/~vandewalle/publications/Festk35,25(1996).pdf